DESIGN OF A LOW-PROFILE RECEIVER FOR A 3.3kW WIRELESS CHARGING CONVERTER

Gautam .H. Pillai

Student Number:5057280

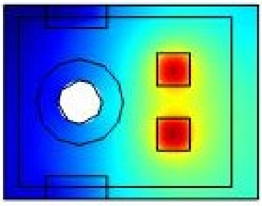

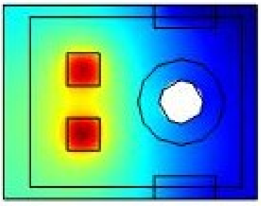

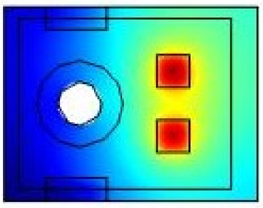

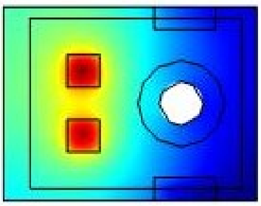

DESIGN OF A LOW-PROFILE RECEIVER FOR A 3.3KW WIRELESS CHARGING CONVERTER

by

Gautam .H. Pillai

to obtain the degree of Master of Science
at the Delft University of Technology,
to be defended publicly on Tuesday August 3, 2021 at 12:20 AM.

Student number:		5057280	
Project duration:		December 3, 2020 – July 31, 2021	
Thesis committee:	Dr. T. Batista Soeiro,	TU Delft, Thesis supervisor	
		Dr. Jianning Dong,	TU Delft
		Dr. Aleksandra Lekic	TU Deflt

This thesis is confidential and cannot be made public until December 31, 2021.

The thesis will available at `http://repository.tudelft.nl/`.

TU Delft

Acknowledgements

This thesis is the result of the work that I have been doing for these few months. Although this is my journey towards the fulfilment of the thesis, there were few others who helped me in achieving my goals. Here I would like to thank all these people who made this thesis possible and a unique experience for me.

I would like to thank Prof. Thiago Batista Soeiro and Prof. Jianning Dong for their patient guidance, encouragement and useful advice on this research work. I would also like to express my deep gratitude supervisor Francesca Grazian for providing me with a unique opportunity to work on this thesis topic. This research would have been incomplete without your valuable guidance, patience and help.

I am also extremely indebted to my thesis committee members and other intellectuals who have contributed in this research work, directly or indirectly. All your valuable pieces of advice, constructive criticism and extensive discussions around my work have helped me in constructing this thesis.

I would also thank my ever supportive friends and colleagues, for being my co-passengers on this exciting journey of 2 years. All of you have been very supportive throughout the way. Your encouragement as well as criticism made the whole masters a memorable one.

I also express my sincere gratitude to the most important people in my life, my parents and my brother. I could not have made it so far without the inspiration and motivation provided by my family. This journey would not have been possible without the prayers and never ending care bestowed by my parents and all my family members. I owe this to you all.

Abstract

The usage of physical space in an Electrical vehicle is a roadblock to achieving peak performance in wireless charging applications. Components like the receiver, onboard power electronics, etc. have to be arranged in such a way that challenges like bulkiness, power density, thermal management is handled to achieve maximum operating life of these devices and their performance. This becomes more prevalent in heavier vehicles. This thesis explores such possibility of solving this constraint by placing the power electronics on top of the receiver.

To start with, different frequency ranges used in Wireless power transmission are discussed, followed by topologies of the coil and compensation networks. Every topology and network has its advantages and disadvantages. And based on various parameters, a comparison is made.

Subsequently, power losses across various components of both the primary and the secondary sides of the Wireless Power Transmission(WPT) are calculated in their worst-case scenarios. These losses are essential for analyzing the thermal management of the system, as these losses produced by the devices generate heat.

A series of thermal models were designed on COMSOL 5.6a to analyze the temperature distributions of these circuits. Starting with a simple model which involves two diodes connected in series to more complex cases like the design of the receiver and finally to the last step which is placing the rectifier on a heatsink atop the receiver. The results are experimentally verified and many conclusions are deduced from them. These results give a better understanding of how heat flows in a system. A thermal analytical model is designed on LT-SPICE to a thermal circuit of arrangement of the components in the system.

Contents

List of Figures

List of Tables

1

Introduction

Over the last couple of decades, there has been a phenomenal rise in the demand for EVs in the fight against climate change. However, there are major challenges that are yet to be addressed in the research and development which impedes its growth. Mainly, the management of energy across the power electronics and systems are still a puzzle to be solved. Constraints like weight, bulkiness, thermal management, battery capacity, space utilisation etc. are just some of the issues, the manufacturers try to solve to make the EVs a better solution than gas powered cars.

To enhance the driving range of EVs, one must add more battery cells and modules. This could further increase the weight and the manufacturing. The Li-ion batteries have comparatively more Energy density and much lighter than other conventional batteries like Lead-ion. Even though Lithium-ion (Li-ion)batteries are used in EVs as the preferred choice for Energy storage system, they have some constraints as well. The energy density of the of Li-ion is much lower compared to gasoline[1]. The raw material lithium is scarcely available, which makes it quite costly. The batteries usually take a lot of time to fully charge. There are some fast battery charging methods that can bring down the battery charging time to as quick as 20–30 min. However, even if energy storage and advanced charging technologies are used, the cost of fast charging systems is expensive.[2].

To solve such constraints a flexible and an efficient solution is needed. The Wireless Power transfer(WPT) technology has proven to be an alternative to the conventional methods where there is a need for a galvanic contact.Wireless charging technology will eliminate the time-consuming process of locating a charging station and attaching the connection for electric vehicles, assuming the cord is not lost or damaged[3]. The WPT avoids the need for a conductive charger by providing great operating flexibility by charging with the set coils attached below the ground for transmission and below the vehicle's chassis for reception. The device can be left alone to charge at any time and in any location without risk of theft or vandalism because the coils are connected by a magnetic field. Dynamic WPT refers to when the car is charged while it is moving. This could reduce the demand of battery capacity by 20 % [1].

An important constraint in wireless charging for electric vehicles is the available space. The receiver coil needs to be within the dimensions of the vehicle's chassis, and the power electronics on board have limited space to perform its necessary operation. As a result, the power density is a major challenge as the automotive manufacturers want compactness and deliver maximum performance. The problem can be solved, by placing the power electronics in an at arrangement on the backside of the coil, such that the aluminum plate used for shielding the magnetic field, can also be used for heat-spreading

To implement the solution for such a problem. Different types of losses are investigated, across all the components on the secondary side of the WPT. A thermal circuit is designed to showcase the analytical model of the system, followed by conducting FEM simulation was to understand the thermal analysis of the system to understand the heat distribution of the system. The results are verified with experiments of the entire WPT system and the differences in the results are analyzed and observed.

1.1. Objective

This research investigates the challenges of placing the rectifier stage of the WPT system together with the heatsink on the backside of the receiver considering the constraints of thermal management and physical space.

1.2. Methodology

To validate this research, one starts with a literature review of the various coil and compensation topologies. Then a list of possible losses across the different components is examined. Subsequently, a simplified structure/packaging model of two commercially available diodes was designed and simulated in COMSOL 5.6a. The result is important in understanding how heat flows in a typical thermal network of a power electronic system, and this model later is used to analyze the final full-bridge rectifier. A methodology for the selection of a suitable heatsink needs to be derived for managing the diodes junction temperature. Followed by, design and simulation of the model of the Receiver pad to understand the heat flow in the structure. Then finally, the combined systems of the rectifier and the receiver pad are simulated to understand the thermal analysis of the entire system. The simulations are verified with experimental results. A thermal model was designed on LT-Spice to give an analytical model of the system.

1.3. Fundamental principles of wireless power transfer

Wireless power transfer can be accomplished in a variety of ways (WPT). One approach of identifying WPT technology is based on the power delivery range[3]:

- Far-field WPT technology:A radiation technique where the wavelength of the electromagnetic waves is in the range of microwaves, laser, and solar radiation.
- Near-field WPT technology: Where the range is in few centimeters, being either capacitive or inductive power transfer (IPT). This can either be purely inductive coupling (PIC) or magnetic resonant coupling (MRC).

For low and medium power levels, IPT with MRC is thought to be quite successful. It is made up mostly of primary and secondary coils, each of which is coupled to a passive compensating network. The circuit runs at a certain resonant frequency, allowing the circuit's reactive power to be compensated by the main magnetic coils.It has been claimed that IPT using MRC has a higher efficiency and can expand the transmission distance compared to IPT using pure inductive coupling.

1.4. Inductive power transfer with magnetic resonance coupling

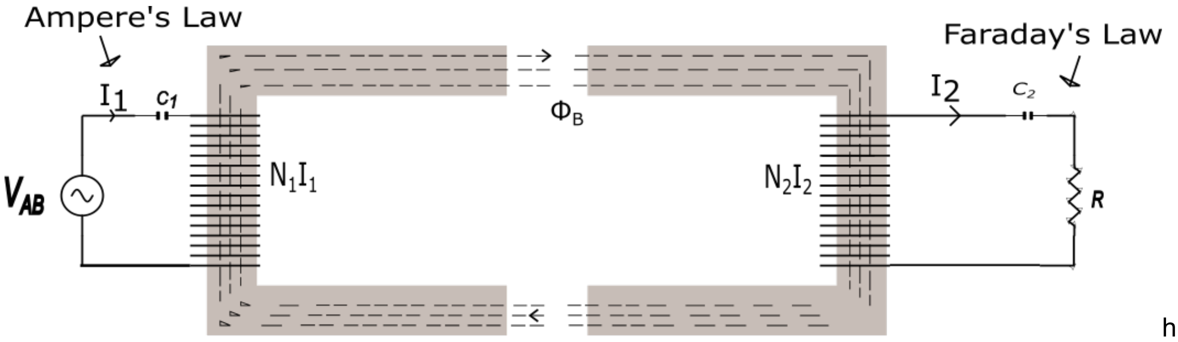

h

Figure 1.1: Fundamental principle of IPT with MRC.

The working principle of IPT can be explained by Ampere's Law and Faraday's Law:

1. *Ampere's law in (1.1)*: The current when it flows through a conductor, it produces magnetic field around it.

$$\int B_T dl = \mu(I_1N_1 - I_2N_2) \tag{1.1}$$

2. *Faraday's law in (1.2)*: When a conductor is placed in a time-varying magnetic field, it induces a voltage.

$$e = -N_2 \frac{d\phi_B}{dt} \tag{1.2}$$

where

- B_T is the magnetic flux density in Tesla (T),
- Δl is the unit length of the conductor in meter(m),
- N_1 is the number of turns in the primary p.u.,
- N_2 is the number of turns in the secondary (p.u.)
- I is the current in primary conductor in Ampere (A),
- ϕ_B is the Magnetic flux in weber (WB).

As shown in Figure 1.1, IPT occurs between two coils separated by a large air gap. Hence, the coupling between both the primary and secondary is loose because of external factors like misalignment between the coils, the presence of foreign objects, etc. The magnetic performance of the coils can be more efficient by placing them close to a material with high permeability to improve the transfer of power. A high-frequency alternating current(AC) flows through the primary coil and generates a magnetic field as defined by Ampere's law. A part of that magnetic field couples with the secondary coil which depends on the coupling, k, and that induces a voltage across the secondary coil according to Faraday's law. Two parameters play a crucial role in power transfer[4]:

1. raising the frequency in order to improve the power transfer capacity
2. the use of capacitors attached to the coils to form a resonant system and enhance transmission efficiency by lowering reactive power to zero.

An IPT system for electric vehicle (EV) charging consists of a transmitter coil connected to the grid is placed either above or below the ground, and a coupled receiver coil placed below the vehicle's chassis. To improve the power transfer, a layer of ferromagnetic materials like Ferrite 3C90 is placed above the coil to direct the magnetic flux path for better linkage. The topmost layer is the thin sheet of Aluminium used for shielding the magnetic effects of the Ferromagnetic and the coil layers. The entire ensemble of the receiver is named a Receiver pad. The transmitter is connected to the grid via an inverter which converts DC to AC. The current flows through the coil and generates a magnetic field around it. The secondary in the presence of the magnetic field produced due to primary induces a voltage and is converted to DC through a rectifier. The DC flows from the rectifier to charge the battery used for the Energy storage.

This type of charging is static because the vehicle is parked during the charging, and in future it will most likely replace systems which require a galvanic contact [4].

When IPT is used for EV charging, there are many issues which concern the manufacturer. It is difficult to operate a magnetic field in the MHz frequency range as the power and efficiency are typically low. It is inefficient to regulate and control power at the level of a few kW to a few hundred kW at MHz frequency level using modern power electronics devices. Moreover,the surrounding ferromagnetic components also effect the performance of the coil. When the coil is attached below the car, the magnetic flux will travel the path with the least magnetic resistance. Hence, the magnetic field lines tend to flow through the chassis causing high eddy current loss as well as a significant influence on the coil parameters and other electronic devices in the vehicles[5].

The static WPT removes the constraint of connecting wires, theft, and vandalism. But the challenges of the power density of a battery make the necessity of the charging stops still a problem. The elimination of mechanical restrictions allows for dynamic IPT research, which involves inductive power transfer while the vehicle is in motion. The implementation of dynamic IPT systems on roadways and highways would eliminate the need for vehicle charging stops. As a result, the on-board battery capacity needs may be reduced, allowing EVs to be lighter and have longer cruising ranges.[2]. The dynamic IPT's successful implementation would increase general acceptance of electric vehicles and address the most pressing issues with their use.

There is a third way which represents a middle ground between the static and dynamic IPT, which can be feasible. It's a variation of stationary IPT, in which the charging happens in places such as traffic signals [1].

1.5. Standardized frequency ranges of the electromagnetic field

Wireless charging has experienced numerous challenges in practical usage until recently, when major manufacturers began to incorporate it into ordinary electronic devices. The most significant impediment it now confronts is the vast diversity of versions of the technology, which makes it difficult for chargers to work with a variety of devices. Hence, for this reason, there are some basic universal standards described in the following sections which define several standards, namely the Qi, Alliance for Wireless Power (A4WP), SAE, and International Electrotechnical Commission (IEC) standards [3].

1. ***The Qi standard***:This standard is mainly used in low power applications, which have a range of up to 5W. Hence, portable devices like mobile phones prefer this standard. The frequencies for the Qi standard vary from 110 to 205 kHz in the low-level range for 0-5 Watts, and 80-300 kHz for medium power ranges like 6-120 W[6]. The distance of wireless transmission according to this standard is up to 40mm[3].

2. ***Alliance for wireless power standard*****(A4WP)**: This standard provides the spatial freedom needed for the wireless charging application. It can generate a larger electromagnetic field with MRC. The A4WP standards have spatial freedom by removing the need for a precise alignment and also allows great separation between the charger and charging devices. The maximum charging distance is in the range of meters, working at 6.78 MHz, the nominal operating frequency[6].The main differences between A4WP and other international standards consist of:

    - *Frequency*:Because high-frequency ranges entail more compact devices, the worldwide unique working frequency of 6.78 MHz was chosen to prevent inductive heating difficulties. As the discharge rate is fast, there is less likelihood of a current build-up. Under much lower frequencies, this is frequent in strongly linked inductive systems.
    - *Control and management protocol*. The type of protocol where the frequency range is inside the international standards used fro applications like smart phones and other devices. [3].

3. ***Society of Automotive Engineers Standard*** **(SAE J2954)**: This standard is mostly used in mainstream applications like as light-duty electric vehicles with operating frequencies in the 79-90 kHz range.[4]. The J2954 standard of the Society of Automotive Engineers (SAE) Task Force governs this. For electric vehicle (EV) applications, an operating frequency of 85 kHz is recommended[6]. Table 1.1 shows the different criteria for different power levels.

Maximum Power Level kVA (At the input)	Z-Class (mm) (Distance between the secondary pad and the ground)	Frequency RangekHz)
WPT1 3.7	Z1 100-150	79-90
WPT2 7.7	Z2 140-210	79-90
WPT3 11.1	Z1 170-250	79-90
WPT4 22		79-90

Table 1.1: Summarization of the J2954 Standard Recommended Practice[1].

SAE J2954 also has standards for the misalignment tolerance for different directions and positions, and the details are given in Table 1.2.

Offset direction	Misalignment tolerance distance(mm)
ΔX	±75 mm
ΔY	±100 mm
ΔZ	$Z_{nom} - \Delta_{low} > Z_{nom} - \Delta_{high}$
Rotation, Roll & Yaw	Testing at +/- 2°,4° and 6°

Table 1.2: J2954 specification on the misalignment distance. [2]

1.6. Common topologies of coils

In most IPT systems, the transmitter(TX) and receiver(RX) pads transfer power through a medium. The permeability of the specified medium impacts the power transfer.In this thesis, the medium is air.The pads are referred as magnetic couplers and facilitate the transfer of power.There are many variables which impacts the performance of the both pads like:

- System coupling coefficient k: It is the portion of the magnetic flux produced from one coil that links with another coil.
- Quality factor Q:It is the ratio of the power stored and power dissipated.
- Misalignment tolerance:The areas of the coil of both transmitter and receiver when are not properly aligned against each other can affect the transfer of power.
- Coil-to-coil efficiency:The ratio of power generated in the transmitter to the power transferred to the receiver.
- Stray/fringe magnetic fields: External magnetic fields like presence of the other electronic devices, or the earths magnetic field.

. Hence, to remove the challenges placed by these constraints, the researchers have come up with specifically designed pad structures that optimize the aforementioned parameters. Magnetic couplers usually are made of Litz wires to mitigate the skin effect in the winding, Ferrite coresare used for improving the mutual inductance by controlling the direction of flux and minimize the leakage inductance, and an Aluminum shielding to avoid effect of magnetic flux on other electronic components inside the EV [1].

Figure 1.2 shows the classification of the most used magnetic couplers based on their basic structure. Magnetic couplers can be classified into:

1. Single-sided or planar pads
   (a) Single-coil pads
      - Circular pads (CPs) in Figure 1.3(a): used mostly in stationary WPT as it has high efficiency and low leakage field.
      - Rectangular pads (RPs) in Figure 1.3(b): Preferred in dynamic WPT as it has high efficiency and low leakage field.
      - Double D (DD) pads in Figure 1.3(c): A DD pad can produces a parallel flux component with a high horizontal misalignment tolerance.

   (b) Multi-coil pads
      - DD-Quadrature (DDQ) in Figure 1.3(d): A DDQ pad consists of the union of a DD pad and an RP. Because of its dual nature, it is operate with other coil topologies and offers high misalignment tolerance. In some cases, it requires two synchronized inverters for powering both coils [3].
      - Bipolar (BP) pads: A BP pad consists of two RPs partially overlapped such that they are mutually decoupled. It is can operate with other pads and offer better misalignment tolerance. In some cases, it requires two synchronized inverters for powering both RPs.

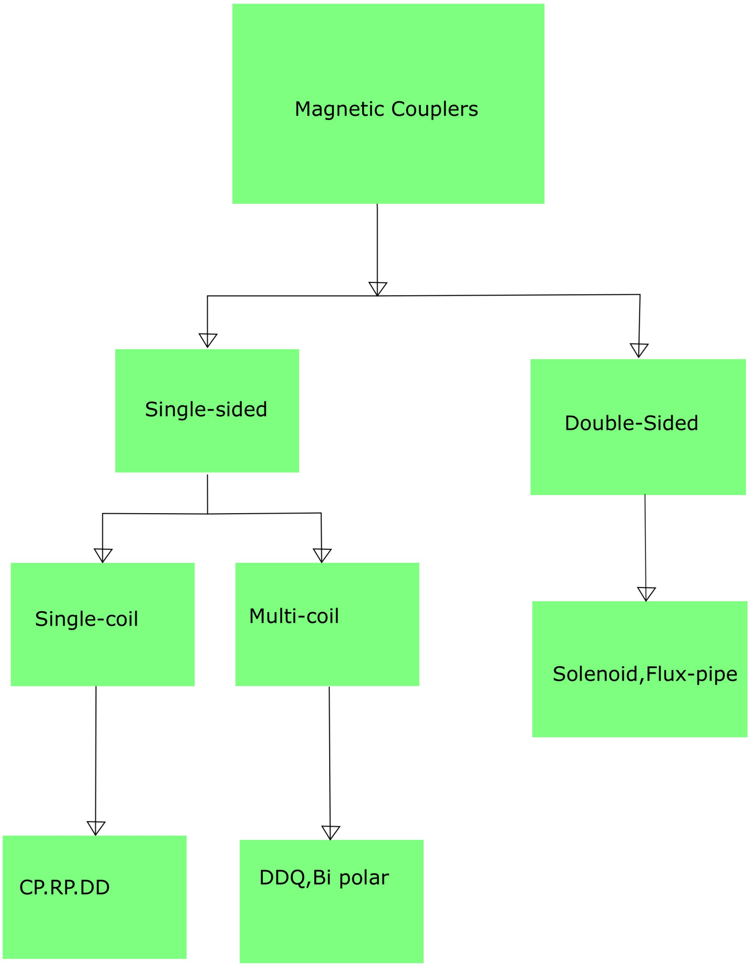

Figure 1.2: Pad topologies classification.

The most common question that industry designers are asked is what type of pad structure will be best for the application. A comparison of different geometries under various conditions has been demonstrated in numerous studies. Researchers have utilized factors such as the coupling factor k to compare different designs, while others have used Q as the criterion in some circumstances. Magnetic couplers should be operated under similar conditions to ensure a just comparison between different structures[7]. In [7], Four topologies are compared are: 1) CP; 2) RP; 3) DD-DD; and 4) DD-DDQ. Each geometry is designed to maximize parameters like coupling coefficient, efficiency,energy density and misalignment tolerance. Some of the important observation deduced from the results are listed in the set of points below:

- CP and RP outperform other pads at the same power densities.
- CP uses the more ferrite and less copper when compared to other pads for the same performance.
- For the same performance, CP employs the most ferrite and the least copper.
- When compared to polarized pads, the CP and RP have reduced stray fields[1].

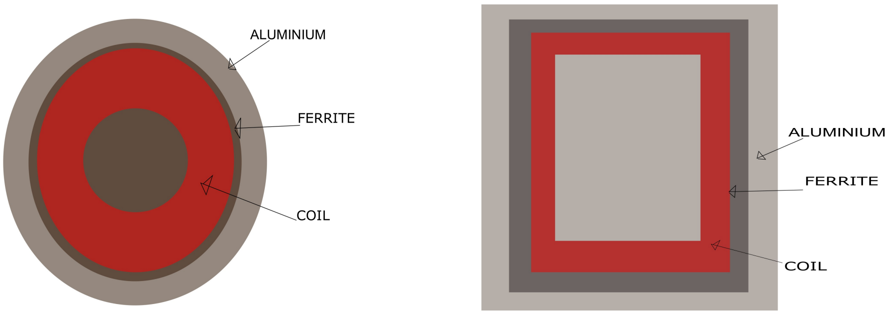

(a) Circular Pad (CP) (b) Rectangular Pad (RP).

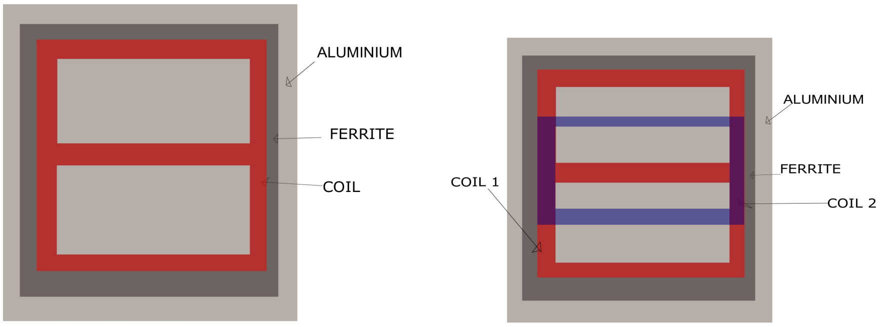

(c) Double D (DD) Pad. (d) DD-Quadrature (DDQ) Pad.

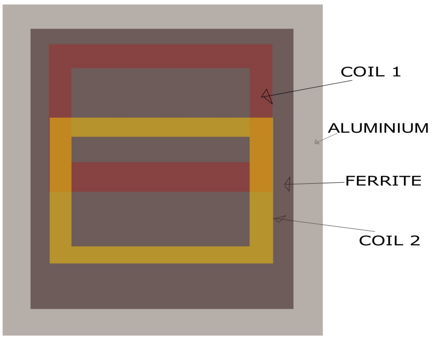

(e) Bi-polar (BP) Pad.

Figure 1.3: Most common coil topologies used in EV wireless charging.

1.7. Compensation networks

The WPT involves transferring power without a mechanical contact. The structure of the WPT like in Figure (1.1), closely resembles a transformer which is loosely coupled. This is due to the large air gap between them. This creates flux leakages and interference of external magnetic fields which impacts the performance of the transformer. This means that the magnetizing flux is significantly low, which results in a much lower magnetizing inductance and mutual inductance [6]. The requirements in the design of compensation network can be described as follows[8]:

- Minimize the Volt-Ampere rating and maximize the power transfer capability.
- Constant-voltage or constant-current output behavior.

- High efficiency.

Types of compensation networks

There are 4 basic compensation networks as shown in Figure (1.4). These are named as Series-Series (SS), Series-Parallel (SP), Parallel-Series (PS), and Parallel-Parallel (PP) based on the connection to the compensation capacitor with respect to the main magnetic coils. The common parameters in these four circuits include

1. L_1: the self-inductance of the primary coil
2. L_2: the self-inductance of the secondary coil
3. C_1: is the compensation capacitor of the primary circuit
4. C_2: is the compensation capacitor of the secondary circuit
5. R_1 and R_2: the lump parasitic resistances of the circuit primary and secondary circuits respectively..

The parallel compensation networks have current sources, while series compensation networks have voltage sources. The key feature of having a compensation network is to minimize the reactive power transfer from primary to secondary coil. Hence, one calculates the primary and secondary parameters by determining the circuit equivalent input impedance Z_{in}.

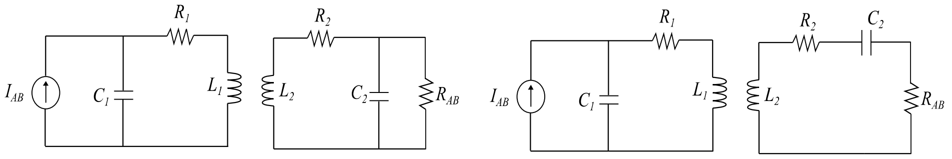

(a) Parallel-Parallel Network (b) Parallel-Series Network

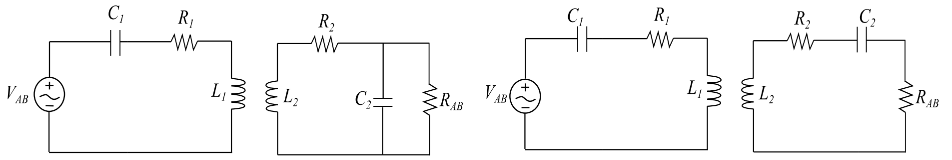

(c) Series-Parallel Network (d) Series-Series Network

Figure 1.4: Most common compensation topologies used in EV wireless charging.

1.7.1. Computation of Z_{in}

The input impedance of the circuit is calculated by analysing the equivalent circuit from the input side of the primary circuit. In order to calculate the input impedance, one determines the reflected impedance which can be calculated by the ratio of the reflected voltage and the primary current as:

$$Z_r = \frac{\omega^2 M^2}{Z_s} \tag{1.3}$$

where Z_s is the secondary impedance and M is the mutual inductance of the primary and secondary coil, which is calculated as

$$M = k\sqrt{L_1 L_2} \tag{1.4}$$

where k is the coupling coefficient of the two coils which varies between 0 and 1. and ω is the operating frequency,

$$\omega = \frac{1}{\sqrt{L_p C_p}} = \frac{1}{\sqrt{L_s C_s}} \tag{1.5}$$

The impedance of the primary side Z_p, depending upon the compensation topology, which can be expressed as:

$$Z_p = j\omega L_p + \frac{1}{j\omega C_p} + Z_r(series) \tag{1.6}$$

$$Z_p = \frac{1}{j\omega C_p + \frac{1}{j\omega L_p + Z_r}}(parallel) \tag{1.7}$$

where Z_s, is the impedance of the secondary network which depends again on the compensation network just like Z_p. Hence Z_s can be expressed either:

$$Z_s = j\omega L_s + \frac{1}{j\omega C_s} + R(series) \tag{1.8}$$

$$Z_s = j\omega L_s + \frac{1}{j\omega C_s + \frac{1}{R}}(parallel) \tag{1.9}$$

Selection of C_p

As mentioned in the previous section, the selection of primary capacitance depends upon the calculation of the input impedance of the circuit. The selection of the primary capacitor C_p has to be performed such that the imaginary power transferred is zero. In order to achieve that, the imaginary part of the Z_P is kept zero.

$$Im(Z_p) = 0 \tag{1.10}$$

By substituting 1.3 and 1.8, the reflected real and imaginary part of the reflected impedance for a series compensated secondary network is:

$$ReZ_r = \frac{\omega^4 C_s^2 M^2 R}{(\omega^2 C_s L_s - 1)^2 + \omega^2 C_s^2 R^2} \tag{1.11}$$

and

$$ImZ_r = \frac{-\omega^3 C_s M^2 (\omega^2 C_s L_s - 1)}{(\omega^2 C_s L_s - 1)^2 + \omega^2 C_s^2 R^2} \tag{1.12}$$

where the operators ‘Re’ and ‘Im’ represent the real and imaginary parts of the reflected resistance, respectively. Then just like that in the case of parallel topology, one would get:

$$ReZ_r = \frac{\omega^2 M^2 R}{R^2(\omega^2 C_s L_s - 1)^2 + \omega^2 L_s^2} \tag{1.13}$$

and

$$ImZ_r = \frac{-\omega^3 M^2 [C_s R^2 (\omega^2 C_s L_s - 1) + L_s]}{R^2(\omega^2 C_s L_s - 1)^2 + \omega^2 L_s^2} \tag{1.14}$$

Therefore from the equations 1.12-1.14, the primary capacitor is calculated according to different common topologies is presented below in Table 1.3

Analysis of Compensation Topologies

To understand the details basic compensation networks, The basic equations and the results of the comparison are listed in the Table 1.3.

In [6],The values of L and C are selected such that the circuit achieves resonance. These components depend on parameters like topology, quality factor, and the coupling coefficient. The choice of the topology has a heavy influence on the choice of a primary capacitor. This can be seen in the comparison of the SS with the SP parameters

The selection of a topology widely depends also on the type of application. For high voltage applications, A series compensation is the preferred choice for applications like a long primary track. Where the primary circuits are arranged in series, and this allows the voltages in the tracks to be divided and

Topology	Equation
SS	$C_P = \frac{1}{\omega_o^2 L_P}$
SP	$C_P = \frac{1}{(L_P - \frac{M^2}{L_S})\omega_o^2}$
PS	$C_P = \frac{L_P}{(\frac{\omega_o^2 M^2}{R})^2 + \omega_o^2 L_P^2}$
PP	$C_P = \frac{L_P - \frac{M^2}{L_S}}{({\frac{M^2 R}{L_S^2}}^{2}) + \omega_o^2 (L_P - \frac{M^2}{L_S})^2}$

Table 1.3: Primary capacitance C_p for basics topologies [6]

managed within the maximum allowable limits. Whereas, for high current applications the parallel compensation is the suitable option. It is a better option for concentrated windings. A single capacitor at the terminals of the coil is used. When it comes to applications like dynamic WPT, high voltages are preferred. A Parallel compensation is a better option, as the current losses would be lower. While in static WPT, the series compensation is preferred. The SP topology has affects the overall efficiency of the system, where it affects power factor and voltage gain of the system[6].

The primary capacitance of the other two topologies with a parallel primary compensating capacitor, the PS and PP, is calculated using complex formulas. Furthermore, the resonance capacitance is affected by parameters such as the coupling factor and load resistance. PS and PP topologies have higher efficiency and power factor at lower mutual inductance, but they are sensitive to a high load fluctuations and mutual inductance.

$$C_1 = \frac{1}{j\omega L_1} \tag{1.15}$$

$$C_2 = \frac{1}{j\omega L_2} \tag{1.16}$$

$$L = \mu_o N^2 \ln\left(\frac{8R}{a} - 2\right) \tag{1.17}$$

$$M = \frac{\pi \mu_o r_1^2 r_2^2 N_1 N_2}{2d^3} \tag{1.18}$$

where μ_o is the magnetic permeability in vacuum. r_1 and r_2 are the radius of the Transmitter coil and Receiver coil, respectively. N_1 and N_2 are the turns of the Transmitter and Receiver coil, respectively. a is the diameter of the wire and d is the distance between the Transmitter coil and Receiver coil.Furthermore, the normalized frequency (u) is defined as:

$$u = \frac{\omega}{\omega_o} \tag{1.19}$$

The normalized load impedance's for series compensated primary systems can be determined as functions of Q_P and Q_S and u by dividing the real and imaginary components of 1.8 and 1.9 respectively by the reflected resistance at the resonant frequency. The real and imaginary components of the normalized load impedance are:

Secondary Compensation	Reflected Resistance	Reflected Resistance
Series	$\frac{\omega_o^2 M^2}{R}$	0
Parallel	$\frac{M^2 R}{L_2^2}$	$\frac{-\omega M^2}{L_2}$

Table 1.4: Reflected resistance and reactance at the secondary resonant frequency [9]

$$\frac{ReZ_t}{ReZ_{r0}} = \frac{ReZ_r}{ReZ_{r0}} \tag{1.20}$$

The terms in 1.20 are given in the Table below:

Topology	Term	Function
SS	$\frac{1}{\omega C_1(ReZ_r0)}$	$\frac{Q_p}{u}$
SP	$\frac{1}{\omega C_1(ReZ_r0)}$	$\frac{1}{u}(Q_p - \frac{1}{Q_S})$
PP	$\omega C_1(ReZ_r0)$	$\frac{1}{u}(Q_p - \frac{1}{Q_S})$

Table 1.5: Normalized functions of the first terms in $\frac{ImZ_t}{ReZ_r0}$ and $\frac{ImY_t}{ReZ_r0}$ [9]

Secondary Compensation	Term	Function
Series	$\frac{ReZ_r}{ReZ_r0}$	$\frac{u^4}{(u^2-1)^2Q_S^2+u^2}$
	$\frac{ImZ_r}{ReZ_r0}$	$\frac{-u^3(u^2-1)Q_S}{(u^2-1)^2Q_S^2+u^2}$
	$\frac{\omega L_P}{ReZ_r0}$	uQ_P
Parallel	$\frac{ReZ_r}{ReZ_r0}$	$\frac{u^2}{(u^2-1)^2Q_S^2+u^2}$
	$\frac{ImZ_r}{ReZ_r0}$	$\frac{-u^3[(u^2-1)Q_S+\frac{1}{Q_S}]}{(u^2-1)^2Q_S^2+u^2}$
	$\frac{\omega L_P}{ReZ_r0}$	uQ_P

Table 1.6: Normalized functions of the terms in 1.20 [9]

Hybrid Compensation circuit

The basic compensation topologies, discussed in the section 1.7.1, have their varieties of hybrid and more complicated technologies, which have been demonstrated recently. There are combinations like placing two or more capacitors or inductors on one side [6], by placing them in series or parallel. The hybrid topologies (LCL-LCL, LCC-LCC) are known for having high efficiency and offer better coupling and a full range of loading. However, adding inductances and capacitance can come with their stray resistances in these complex topologies which causes further copper losses than SS topology under the rated power, especially for cases of higher power transmission. The description of these hybrid models are described as follows[1]:

1. **LCL Compensation circuit**:

    - LCL has a better light-load characteristics
    - LCL topology can achieve high efficiencies even in worst case scenarios;
    - LCL topology can maintain constant current throughout the entire range from $0 \leq k \leq 1$.

    The parameters of LCL can be determined by the following equation:

    $$\omega = \frac{1}{\sqrt{L_2 C_2}} \tag{1.21}$$

    In this circuit one Inductor L_{f1} is added to the circuit followed by a parallel LC circuit. As the inductor stores energy in the form of electrical field, it can act as a current source. Thus, the LCL can be designed in such a way that the capacitor C_1 is tuned with L_1. Hence one can chose $L_1 = L_{f1}$, so that the circuit becomes resistive. And C_1 is resonant with both L_1 and L_{f1}.

2. **LCC Compensation circuit**:

    - The characteristic of the LCC topology greatly simplifies the control complexity in the primary side;
    - The characteristic of the LCC topology can achieve a unity power factor at the secondary side, which leads to high power conversion efficiency;

- The LCC topology has the characteristic of constant current at both the input and output.

A proper design for the LCC compensation topology for EV charging was presented in [3], which helps in reducing the size of an additional coil, which address issues like compactness and efficiency. The tuning of the LCC circuit is done by first computing the series impedance and primary inductance L_P and C_{f1}:

$$Z_1 = j\omega L_1 + \frac{1}{j\omega C_{f1}} \tag{1.22}$$

Now as Z_1 is an impedance with only imaginary part in it. Thus, If one chooses a frequency which is slightly higher than the resonant frequency it will make Z_1 inductive. Hence one can chose,

$$L_e = L_1 - \frac{1}{\omega^2 C_{f1}} \tag{1.23}$$

And one chooses

$$L_{f1} = L_e \ll L_P \tag{1.24}$$

In this way, the circuit is tunes just like in the case of a LCL compensation circuit. The transferred power is dependent on L_{f1}. Hence, the transferred power can be controlled by tuning L_{f1} accordingly.

2

Simulation of WPT and Estimation of power losses

The WPT solves many issues like reducing the need of charging cords which will have its own losses and costs. It offers high operational flexibility and opens the door towards dynamic power transfer, which brings the advantage that the battery can be charged while the EV is in motion. Although this system has its own perks, it has losses in the coil and in the ferrite layers, there are losses generated in conduction and switching losses in the power electronics. These are primarily dissipated in the form of heat. Hence to understand the thermal analysis and the temperature distribution of the receiver, estimation of the losses is vital. These losses are nothing but the heat sources of the thermal modeling of the system. The equivalent circuit of the system was designed in LT-Spice. The design of the circuit is shown in Figure 2.1.

2.1. Layout of the Wireless power transfer

The WPT system schematic composed of the primary circuit and secondary circuit is shown in Figure 2.1. The primary side consists of the DC input voltage V_{in} connected in parallel to the capacitor C_{in} followed by a DC-AC converter consisting of a full-bridge inverter. The latter is connected to the aggregate of the series-series (S-S) compensation network operating at a resonating frequency of 85 kHz, and coupled coils, which output is connected to a full-wave rectifier that converts the voltage from AC to DC. In this way, the WPT system can be interfaced with a battery that can be modeled as a voltage source.

The receiver coil is of rectangular pad topology, where the wires are made up of Litz. The type of ferromagnetic material used is ferrite 3C90 and the aluminium layer is used as the final shielding layer. The layers stacked up on each other with layers of Medium Density Fibre wood between them as it provides the framework for the receiver pad, its very light and doesn't make the receiver pad bulky.

2.2. Calculation of the losses

The total loss in the entire circuit can be calculated by summing up the losses of the individual components. The parameters in the circuit of Figure 2.1 are as follows:

2.2.1. Calculation of parameters

The voltages and current in primary and secondary circuits are calculated using Kirchhoff equations, which are necessary for the calculation of losses in across different components. The circuit is operating in resonance hence, the inductive and capacitive components cancel each other's reactance out. So the equation in the primary circuit is calculated as:

$$V_{AB} = I_{L1}R_1 + j\omega_0 M I_{L2} \tag{2.1}$$

And the equation in the secondary circuit results in

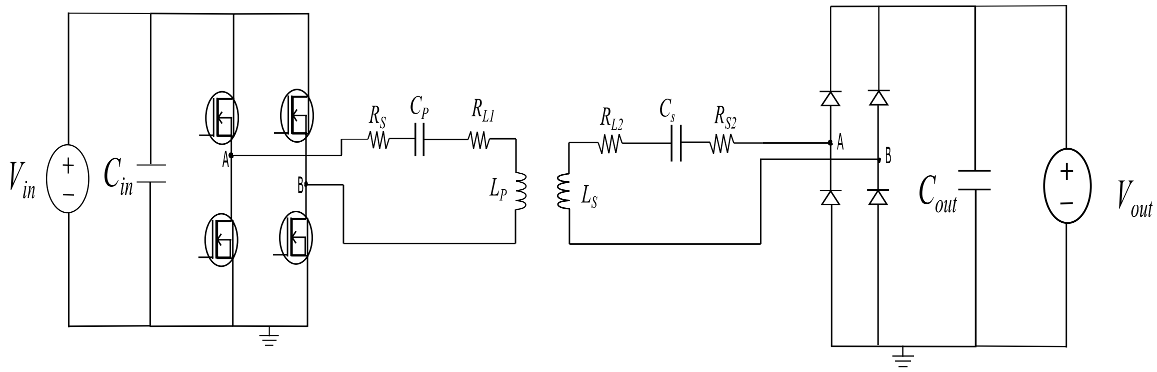

Figure 2.1: Circuit design of SS compensation circuit in LT-Spice XVII.

Parameter	Value(SI unit)
M	90.13 μH
R_{LP}	0.63224 Ω
R_{LS}	0.42683 Ω
L_P	340.66 μH
L_S	219.54 μH
f_0	85 kHz
V_{in}	350-500 V
V_{out}	290-400 V

Table 2.1: Table of parameters in WPT

$$I_{L2}(R_2 + R_{ac}) + j\omega_0 M I_1 = 0 \tag{2.2}$$

where I_1 is the current in the primary circuit, I_2 is the current in the secondary circuit, V_{AB} is the voltage between the terminals A and B after getting converted to AC from the DC input. V_{AB} can be calculated as

$$V_{AB,peak} = \frac{4}{\pi} V_{in} \tag{2.3}$$

The R_{AC} is the AC resistance of the circuit in Figure 1.4 which is related to load resistor R_L by:

$$R_{AC} = R_L \frac{8}{\pi^2} \tag{2.4}$$

And the DC output current I_{out} is defined as

$$I_{out} = \frac{V_{out}}{R_L} = \frac{2}{\pi} I_{2,peak} \tag{2.5}$$

Therefore, using (2.2) and (2.5), the primary current I_1 is:

$$I_{L1} = \frac{j\pi}{2} \left(\frac{I_{out}(R_2 + R_{AC})}{\omega_0 M} \right) \tag{2.6}$$

The device has to be setup in such a way that it operates in a worst case scenario. Hence, the losses are high when the current is the highest. The current will only be high when the load demand is high. Hence, worst case scenario is when V_{out}=400 V.

2.2.2. Losses in the primary circuit

The losses in the primary circuit mainly occur in the inductor and capacitor, due to its resistive components. The power losses in the inductor can be calculated as

$$P_{L1} = I_{L1,rms}^2 R_{L1} \tag{2.7}$$

$I_{1,rms}$ is the rms current of the primary of I_1 and the R_{L1} is the equivalent series resistance pf the primary coil inductor.The capacitor and the inductor coil are connected in series, hence the conduction loss of the capacitor is equal to:

$$P_{C1} = I_{L1,rms}^2 R_{C1} \tag{2.8}$$

where the R_{C1} is the equivalent series resistance of the primary capacitor. The losses in the worst case scenario of the primary inductor and the capacitor are:

$$P_{L1} = 36.16W$$

$$P_{C1} = 2.29W$$

2.2.3. Losses in the secondary circuit

Similarly to the primary circuit, the losses in the secondary circuit mainly occur in the inductor and capacitor, due to its resistive components.The power losses in the secondary inductor can be calculated as

$$P_{L2} = I_{L2,rms}^2 R_{L2} \tag{2.9}$$

$I_{2,rms}$ is the rms current of the secondary current I_2 and the R_{L1} is the equivalent resistance of the primary coil inductor. As the capacitor and inductor coil are in series, hence the conduction loss of the capacitor is equal to:

$$P_{C2} = I_{L2,rms}^2 R_{C2} \tag{2.10}$$

where the R_{C2} is the equivalent series resistance of the secondary capacitor. The losses in the worst case scenario of the primary inductor and the capacitor are:

$$P_{L2} = 35.84W$$

$$P_{C2} = 3.36W$$

2.2.4. Calculation Losses in the inverter

The losses in the MOSFET are mainly of two types. One is the losses due to conduction and the other loss is the one due to the switching mechanisms. The MOSFET chosen for the hardware setup is C2M0040120D, as it has high V_{DS} rating and low on resistance $R_{DS,on}$. The selection of the parameters has to be done in such a way that the device operates in the worst case scenario[10]. The required parameters of the MOSFET from the datasheet needed for the calculation of the losses are:

- $R_{DS,on}$=62 mΩ (at T_j=100 $°C$.)
- E_{off}= 0.1 mJ (for V_{DS}=800 V, I_d=40 A)
- E_{on}= 0 J since the inverter is operated with zero voltage switching turn-on.

The conduction losses happens when the MOSFET conducts and the resistive elements in the device creates the ohmic losses and can be calculated as

$$P_{CD} = R_{DS,on} I_{D,rms}^2 \tag{2.11}$$

where the $I_{D,rms}$ is the RMS of the current through the MOSFET which can be calculated by :

$$I_{D,rms} = \sqrt{\frac{1}{T}\left(\int_0^T i_m(t)^2\,dt\right)} \tag{2.12}$$

Now as the duty ratio D is taken as 0.5, both turn-on and turn-off times are equal. Hence when it comes to operation of a MOSFET in an inverter over a period of time:

$$i_m(t) = \begin{cases} I_{L1} sin(2\pi f_0) & 0 \leq t \leq \frac{T}{2} \\ 0 & \frac{T}{2} \leq t \leq T \end{cases} \tag{2.13}$$

Hence when using the condition in 2.13 to determine the rms current in the Mosfet one gets

$$I_{D,rms} = \frac{I_{L1}}{\sqrt{2}} \tag{2.14}$$

and the switching losses happen when the MOSFET gets turn-on and turn-off during switching at the end of their time periods. In this case $E_{on} = 0J$ as the inverter is operating with Zero voltage switching. Hence, the switching losses can be calculated as:

$$P_{sw} = (E_{on} + E_{off})f_0 = E_{off} f_0 \tag{2.15}$$

Therefore the cumulative losses in the inverter are the combined losses of all the four MOSFET’s

$$P_{inv,loss} = 4 \times (P_{CD} + P_{sw}) \tag{2.16}$$

Hence, the losses in the inverter in the worse case is

$$P_{inv,loss} = 10.59W$$

2.2.5. Losses in the Rectifier

The full-wave bridge rectifier consists of four diodes. The diode chosen for this simulation is the Cree C4D20120H as it can be used for high frequency operation. There are two types of losses which happen in a diode, first is the losses due to switching which occurs when the diode switches on and off during the operation. The switching losses can be calculated as:

$$P_{sw} = E_{rr} f_0 \tag{2.17}$$

Where E_{rr} is the reverse recovery energy. As in this rectifier Voltage and current are in phase, where the switched current is close to zero, and the device technology is SiC the E_{rr} is negligible. This implies that, P_{sw} is zero [10].

The second type of loss is due to the conduction which occur when the diode is in forward conduction mode due to the on-state voltage drop (V_F).The required parameters of the Diode from the datasheet needed for the calculation of the losses are:

- Forward resistance of the diode R_D=68 mΩ
- Forward voltage drop U_{d0}= 0.6 V

The conduction losses has two parts in the equation below first term is due to the ohmic losses in the diode and the second term is due to forward voltage drop.

$$P_{CD} = R_D I_{d,rms}^2 + U_{d0} I_{d,avg} \tag{2.18}$$

where the $I_{d,rms}$ and $I_{d,avg}$ is the RMS of the current through the diode. $I_{d,rms}$ and $I_{d,avg}$ can be calculated by:

$$I_{d,rms} = \sqrt{\frac{1}{T}\left(\int_0^T i_d(t)^2\, dt\right)} \tag{2.19}$$

$$I_{d,avg} = \frac{1}{T}\int_0^T i_d(t)\, dt \tag{2.20}$$

As duty ratio D=0.5, hence

$$i_d(t) = \begin{cases} I_{L2} sin(2\pi f_0) & 0 < t \leq \frac{T}{2} \\ 0 & \frac{T}{2} < t \leq T \end{cases} \tag{2.21}$$

Hence using the condition in 2.21. We get $I_{d,rms}$ and $I_{d,avg}$ as:

$$I_{d,rms} = \frac{I_2}{2} = \frac{\pi}{4} I_{out} \tag{2.22}$$

$$I_{d,avg} = \frac{I_2}{\pi} = \frac{I_{out}}{2} \tag{2.23}$$

Therefore the cumulative losses in the inverter are the combined losses of all the four Diode’s

$$P_{rect,loss} = 4 \times (P_{CD} + P_{sw}) \tag{2.24}$$

And hence the worst case scenario when the rectifier loss is at its highest is:

$$P_{rect,loss} = 4 * 5.33 = 21.32W$$

The comparison of losses was done for different values output voltage V_{out} using at MATLAB and LT-Spice, and the losses are compared for both the software in the Appendix-A .

3

Thermal Analysis

In sections 2.2.4 and 2.2.5, the different types of losses in the system which are responsible for generating the heat in the system were modeled. There are mainly three types of heat transfers which happen in any system. These are conduction, convection and radiation. Conduction occurs when energy is transferred between two objects that are in physical contact. The thermal conductivity k, which is a material's ability to conduct heat, is the most important variable in conduction and it is evaluated primarily in terms of Fourier's Law for heat conduction in (3.1).

$$\dot{Q} = \frac{l}{kA}(T - T_\infty) \tag{3.1}$$

Where in (3.1), l is the length of the layer in the direction of heat flow, A the area of cross-section perpendicular to the direction of heat flow, T the temperature of the layer and T_∞ is the external temperature.

Convection occurs when energy is transferred between an object and its surroundings as a result of the motion of the surrounding fluid. In this project it is the transfer of heat between the receiver pad and the rectifier to the air. The main variable which determines the convection of heat is the heat transfer coefficient h, which depends on certain factors like geometry of the object, density, heat capacity etc. And finally, the Radiation which is the transfer of heat by emission of electromagnetic radiation.

The third case i.e. radiation is negligible as the power level of the losses is not high enough for a significant radiation to happen. Hence, the main types of heat transfer which majorly contribute are the first two types i.e. conduction and convection. The thermal analysis of the system was done by using the finite element method (FEM) in COMSOL Multiphysics 5.6a.

To have a proper working FEM model of the receiver pad and the rectifier, one should start with simple cases and models and then slowly and gradually progress to the complex cases to understand the flow of heat. There are many range of factors to be considered in creation of an FEM model like starting from the designing of a diode, designing of the rectifier arrangement, understanding the heat transfers in the different components like coil, ferrite and selection of an effective heatsink.

3.1. FEM

The finite element method (FEM) is a useful tool for handling problems such as thermal analysis and fluid dynamics analysis. In general, an engineer attempts to analyze the distribution of a certain parameter, such as temperature or heat flux in thermal analysis, electrical charge in electrical analysis, and so on. To analyze heat flows and temperature distributions, known conditions and laws are applied to the geometry.[11].

3.1.1. Design of a diode

The basic function of a diode is to be one-direction switch for the current. In a practical scenario the diode is built and packaged in a mold by the manufacturer following a specific standard. In the case of the diode C4D20120H, it is made with the structure known as TO-247-3 packaging like illustrated in Figure 3.2. The selected diode consists of two chip dies. The internal framework of the diode is

Figure 3.1: C4D20120H.

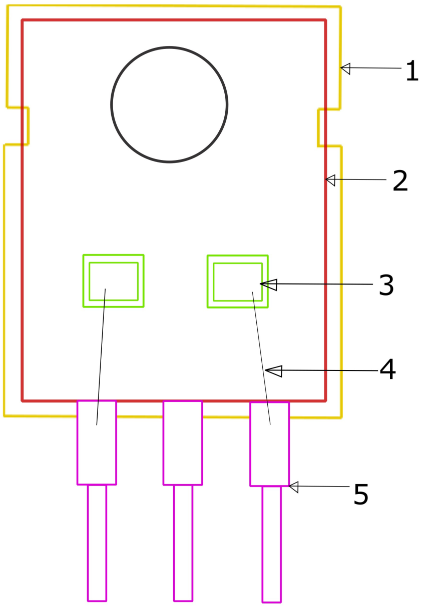

Figure 3.2: Internal structure of TO-247 package for C4D20120H diode[12].

shown in Figure 3.3. The chips consists of two parts, die frame and die pad opening are placed at a distance of x mm from each other. The die frame is made of Aluminium and diode pad opening which is the anode in the Silicon Carbide (SiC) semiconductor.

The die structure consists of multiple layers which are essential for both the flow of current and transfer of heat. The layers consist of coating of aluminium of $4\mu m$ thickness, as its a good conductor of heat and electricity. It facilitates the transfer of heat from the die to the mold. The total die thickness is of 370 μm and below the die is the die attach which is a paste used for attaching the die frame to the base of the chip. The materials of the layers of the die are described in table 3.2.

3.1.2. Design of the heatsink

The heatsink is a component that transfers heat from the higher temperature device to a lower temperature external fluid. Usually a heatsink could be a fan or flat heatsink made of aluminium. In this thesis, a flat heatsink is preferred as the power losses are in the range 0-10 W for the diodes. A heatsink usually works by absorbing the heat generated by the source, i.e. the heat flows in the heatsink and away

No	Item	Material
1	Mold compound	Flame-retardant Epoxy Resin
2	Lead frame	Base material: Copper Alloy
3	Die	Silicon Carbide
4	Bond wires	Aluminium
5	External plating	Solder (Sn)

Table 3.1: Table of materials for different parts of the diode:C4D2012H

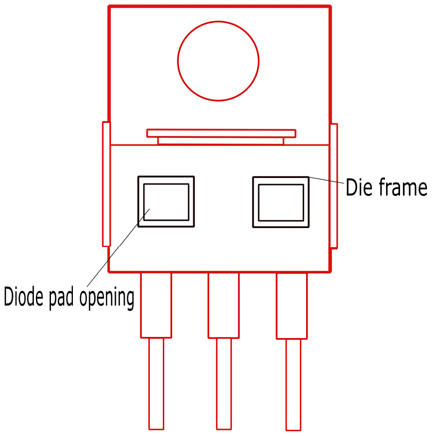

Figure 3.3: internal structure of the diode C4D20120H[12].

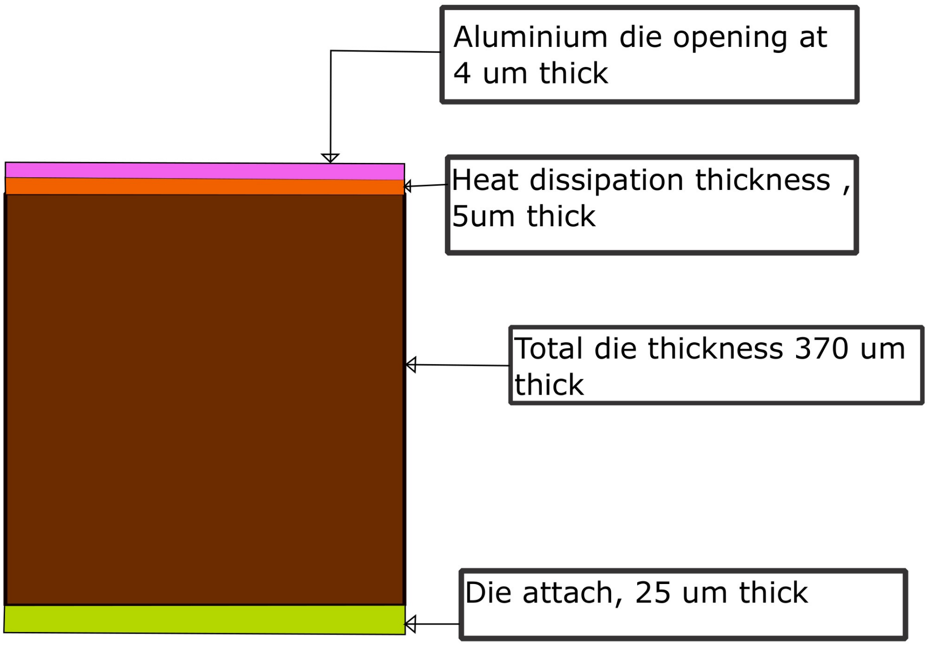

Figure 3.4: Layers of die[12].

from the source due to natural thermal conduction. The heatsink material's thermal conductivity plays an important role in this process hence, conductors like Aluminium or copper. The heat distributes

Material	Part of the component	Conductivity	Specific heat capacity	Density
Mold Compound	Over mold	0.9	669	1900
J-Alloy	Die attach	55	167	7800
SiC	Die	411	760	3210
Copper	Leads,die flag	385	385	8930

Table 3.2: Material properties of the die layers

throughout the heatsink and travels from the region of high temperature to the region of low temperature. This means that the heatsinks temperature distribution is not consistent, hence the temperatures are higher near the source and lower towards the edges of the heatsink close to the cooling material. And the last stage is convection, where the fluid in the case, the air. The air passes across the surface of the warm heat sink and the temperature of the air rises due to which convection takes place.

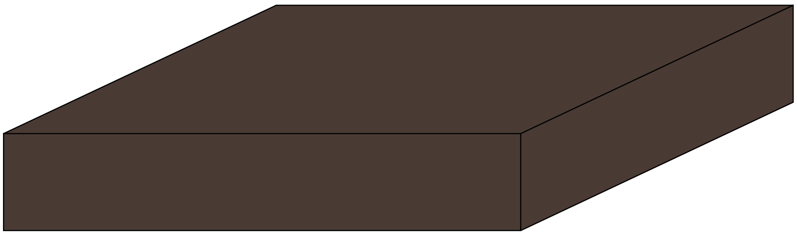

Figure 3.5: Design of flat heatsink

3.1.3. Design of the Receiver Pad

The receiver pad is an vital component in the operation of the WPT. The receiver pad consists of three essential components which are the litz coil, the ferrite layer and the top layer of aluminium shield. These three layers are surrounded by wood MDF, as its low density and is primarily used for framing the layers and provide a support framework for the layers just like shown in Figure 3.7 and Figure 3.8. The coil layer consists of wires made of litz arranged in rectangular planar (RP) coil as it has comparatively low leakage field and high efficiency. The ferromagnetic layer is of ferrite 3C90, a material with high permeability and high thermal conductivity. This is mainly used for directing the flux path such that there is less flux leakage and consequently more power transmitted. But in thermal analysis the heat always follow the path of low thermal resistance, as higher the temperature gradient more is the heat flow, hence a layer of ferrite can be an effective pathway for the removal of heat. The aluminium shield is mainly used for extracting the heat generated from the losses in the coil and also in the power electronics.

3.2. FEM Simulations results

The FEM simulations for the model are conducted using the COMSOL 5.6a to analyse the flow of heat in the receiver pad. The approach is done simulating each component of the system individually, to late verify the analysis experimentally. As this thesis mainly focuses on thermal analysis aspect of wireless power transfer, the type of physics package used in COMSOL 5.6a is Heat Transfer in Solids. To simulate a heat transfer problem, one needs to understand the following equation below:

$$q = h(T - T_{ext}) \tag{3.2}$$

where h is a heat transfer coefficient and T_{ext} the temperature of the external fluid at room temperature.

The heat transfer coefficient is an important parameter in deciding the flow of heat in a body. If the geometry is complex then it could be complicated to designate a specific value of heat transfer coefficient. The coefficient h is dependent on multiple factors, such as the fluid's viscosity, and the surface temperature. In addition, the geometrical configuration affects the coefficient. And geometry's properties like density, heat capacity, etc, also play a role. Hence, in such cases it is recommended

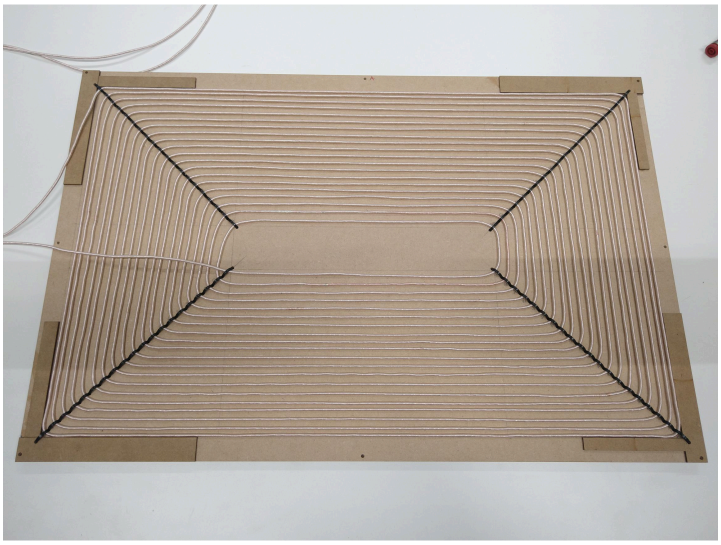

Figure 3.6: Litz wire coil arrangement.

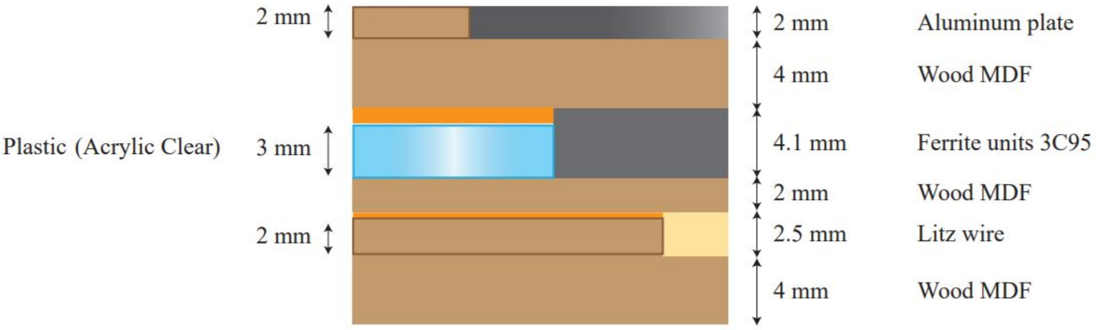

Figure 3.7: Layers of the Receiver

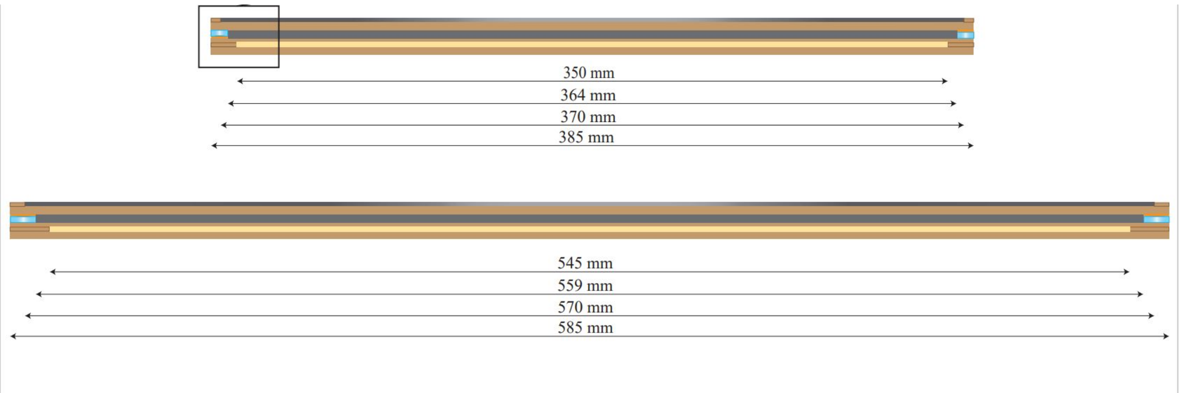

Figure 3.8: Dimensions of the Receiver

to extend the model the way to describe the heat flow and transfer in the surrounding fluid. There are empirical formulas and equations which help acquiring the accurate and efficient result [13]. Therefore, these equations are based on the dimensionless integers in the table below:

1. the Nusselt number, $Nu_L = hL/k$;

2. the Reynolds number, $Re_L = \rho UL/\mu$;
3. the Prandtl number, $Pr = \mu C_p/k$;
4. the Rayleigh number, $Ra_L = Gr_L Pr$;

where,

- h is the heat transfer coefficient (W/(m.K));
- L is the characteristic length (m);
- δT is the temperature difference between the surface and the external fluid bulk (K);
- g is the acceleration of gravity ($m^2 s$);
- k is the thermal conductivity (W/(m.K));
- ρ is the fluid density (kg/m^3);
- U is the bulk velocity (m/s);
- μ is the dynamic viscosity (Pa.S);
- C_p is the heat capacity at constant pressure of the fluid. (J/(kg.K)).

The Reynolds number, Re_L, describes the ratio between inertial and viscous forces when forced convection is present. In the case of natural convection, however, the velocity is uncertain because the flow of air has no defined velocity. In these situations, the Grashof number comes in handy for defining the flow. The Grashof number is calculated as follows:

$$Gr_L = \frac{g\rho(\rho_{ext} - \rho_s)L^2}{\mu^2} \tag{3.3}$$

where g denotes gravity's acceleration, ρs the density of the heated surface, p_{ext} the density of the free stream, L the length scale, μ the fluid's dynamic viscosity, and ρ its density.

All differences in fluid characteristics are accounted for by the Grashof number. When the density of a fluid is affected by its temperature, such as dry air. The grashof number in this situation is:

$$Gr_L = \frac{g\alpha_p(T_s - T_{ext})\rho(\rho_{ext} - \rho_s)L^3}{(\mu/\rho)^2} \tag{3.4}$$

Where α_p is the coefficient of thermal expansion is given by:

$$\alpha_P = -\frac{1}{\rho}\left(\frac{\partial\rho}{\partial T}\right)_P \tag{3.5}$$

which for ideal gas becomes:

$$\alpha_P = \frac{1}{T}$$

Validation of a simplified COMSOL model with experimental results

In this step, a simplified model of two diodes connected in series is considered so that the preliminary step would be to understand how heat flows, and later more complex cases can be built from here. The geometry of this model is shown in Figure 3.9 and Figure 3.10. The diode is designed in accordance with the TO-247-3 package just like the one depicted in Figure 3.2. In order to perform FEM-based simulation, implement the right physics is essential. The first important step is identifying the location of the heat source, hence as the chips inside the diode are mainly responsible for the operation of the chip hence the heat losses originate from there.

To decide the accurate value of the heat transfer coefficient, it is essential to understand the flow of heat in the diode. The heat as it originates from the pair of chips could either flow from the chip to the top of the package or it could flow from the chip to the bottom or case of the package and exit

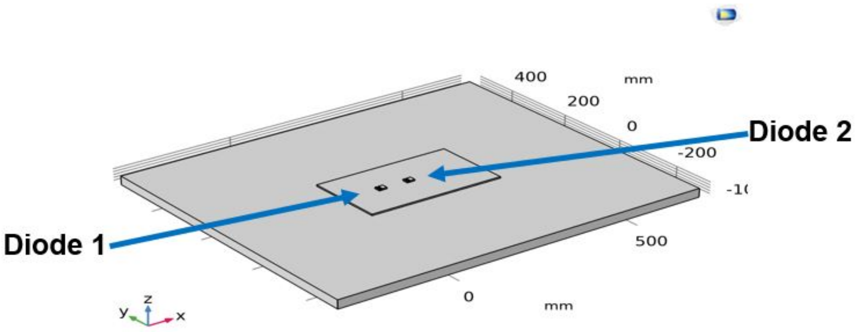

Figure 3.9: COMSOL model of two diodes in series.

through a heatsink. The top case of the diode could be considered as a flat plate, where the air is at room temperature. When the cold air comes in contact with the warm surface of the diode, convection happens where the air absorbs the heat and rises. In such cases, where such a correlation happens, then the corresponding equation is [14]:

if $\rho < \rho_{ext}$

$$h = \begin{cases} \frac{k}{L} 0.54 Ra_L^{\frac{1}{4}} & if 10^4 < 0.54 Ra_L \leq 10^7 \\ \frac{k}{L} 0.15 Ra_L^{\frac{1}{3}} & if 10^7 < 0.54 Ra_L \leq 10^{11} \end{cases} \tag{3.6}$$

Now if, $\rho > \rho_{ext}$

$$h = \frac{k}{L} 0.27 Ra_L^{\frac{1}{4}} if 10^5 < 0.54 Ra_L \leq 10^{10} \tag{3.7}$$

where:

- ρ is the density of the respective material;
- Ra_L is the Rayleigh's number a parameter which is an indicator for the flow of heat;
- k is the thermal conductivity of the material.

Moreover, the characteristic length L of the diode geometry is

$$L = \frac{Area}{Perimeter} = \frac{E \times D}{2 * (E + D)} \tag{3.8}$$

where:

- length of the the diode E=16.13 mm;
- and breadth of the the diode D=21.10 mm.

When the heat flows from the junction to the lead frame and then to the Aluminium pad, the boundary between the two solids is not usually smooth. The boundaries have air gaps which are bad conductors of heat and hence the transfer of heat is not smooth. In such cases, these boundaries are filled with rectangular structures called thermal pads, which are essential in removing the air gaps due to rough surfaces between them and ensures smooth transfer of heat. In the simulation, modeling such thermal pads as geometry can be very difficult. These structures have a thin thickness and are difficult to model as the meshing involved for such thin geometries can be difficult as it will create inaccuracies in the results.

When designing a diode, there are three places where a thermal interface material is necessary for the efficient transfer of heat energy. The first one is the anode pad opening coated with aluminum. Secondly, the diode attach below the chip, and last, the third layer is the Polyimide placed below the diode for the transfer of heat from the diode to the heatsink. The materials of these layers are listed in Table 3.3 with their respective properties.

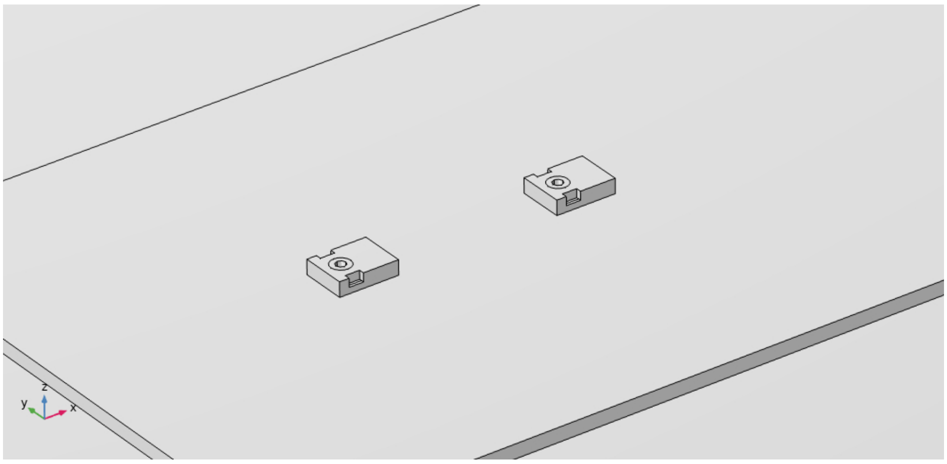

Figure 3.10: closer look of the two diodes.

Material	Thermal Conductivity (W/(m.K))	Thickness(m)
Polyimide	0.15	0.1 mm
Aluminium	240	$4\mu m$
Diode attach	55	$25\mu m$

Table 3.3: Properties of Thermal Interface Materials

These materials provide an effective interface for the transfer of heat, while there can still be a minute thermal resistance that could help in the temperature rise. The thermal resistances of the Polyimide can be calculated as

$$R_{th,p} = 0.107 \circ Cin^2/W$$

where $R_{th,p}$ is thermal resistance per unit area of the Polyimide sheet. Hence the thermal resistance of the entire area occupied by the one sheet of Polyimide is:

$$R_p = R_{th,p} \times E \times D * 1.05 = 2.467 \times 10^{-8} \circ C/W$$

Just like that, in the case of diode attach, the thermal resistance per unit area $R_{th,a}$ is:

$$R_{th,a} = 1 \times 10^{-6} \circ Cm^2/W$$

Hence, the thermal resistance of the entire area occupied by the diode attach is:

$$R_a = R_{th,a} \times 2.7 \times 10^{-3} \times 2.7 \times 10^{-3} \circ C/W$$

Three cases are taken into consideration for different power levels P=10 W,30 W and 40 W, and their junction and top-case temperature were observed. The diodes are placed at a distance of 75 mm apart from each other. The pair is placed on an aluminum plate with dimensions of 360mm x210mm and a thickness of 5mm. The system is placed on a block of wood large enough for heat transfer, as in practice the system is placed on a wooden table. Since the heat flows from the diodes to the aluminum plate, there will also be a heat transfer coefficient designated to the plate. Hence, (3.2) and (3.3) play an important role in determining the heat transfer coefficient. The characteristic length L_{AL} in the case of the aluminium plate is:

$$L_{AL} = \frac{Area}{Perimeter} = \frac{(l_{AL} \times h_{AL} - 2 \times E \times D)}{2 \times (l_{AL} + h_{AL})}$$

where:

- l_{AL}=360 mm is the length of the aluminium plate;
- D=210 mm is the breadth of the aluminium plate.

Therefore,

$$L_{AL} = 0.06572m$$

Since the area of the diodes is taken into consideration, the total area occupied by the two diodes would be $2 \times E \times D$. Just like that same as in the case of the wood table where the characteristic length L_{wood} is:

$$L_{wood} = \frac{Area}{Perimeter} = \frac{(l_{wood} \times h_{wood} - l_{AL} \times h_{AL})}{2 \times (l_{wood} + h_{wood})}$$

where:

- length of the wooden table considered l_{AL}= 1 m=1000 mm;
- and breadth of the wooden table D=210 mm.

Therefore,

$$L_{wood} = 0.20772m$$

In the practical scenario, the wooden table is very long and, in the simulation, the length of the table is also considered. The results of the COMSOL simulation are as shown in Figure 3.11 and Figure 3.12.

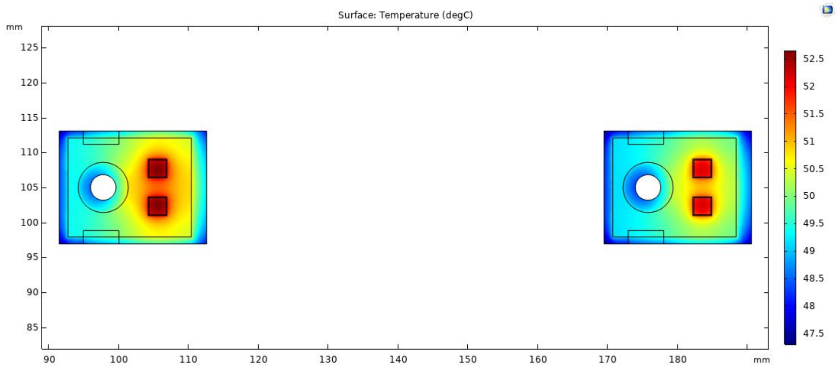

Figure 3.11: Temperature distribution for the junction for P=10W.

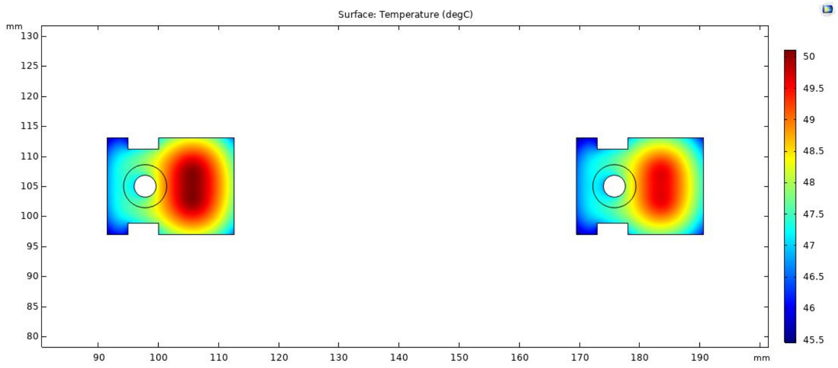

Figure 3.12: Temperature distribution of the top case of the diodes for P=10W.

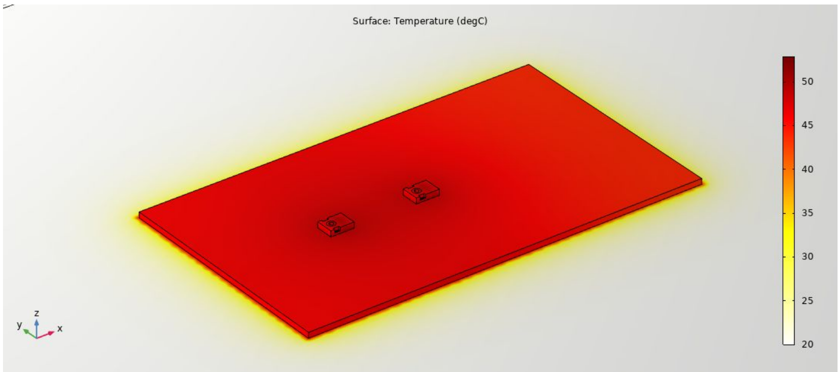

Figure 3.13: Temperature distribution the two diodes for P=10W.

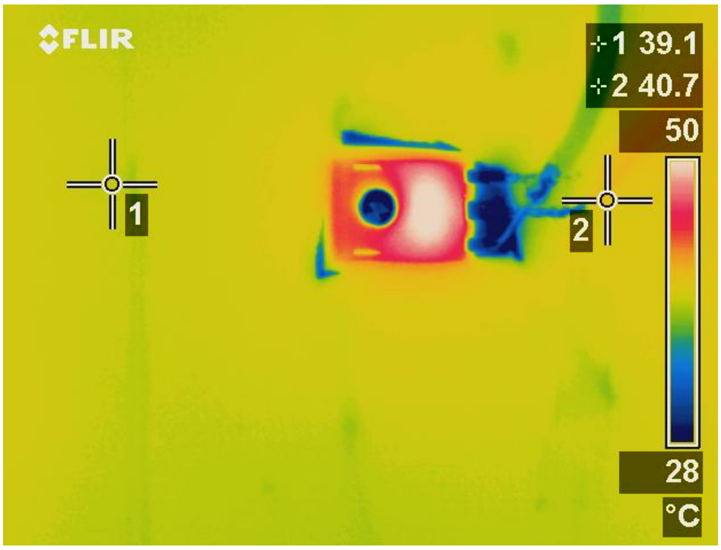

Figure 3.14: Experimental Temperature distribution of the diode 1 at P=10 W.

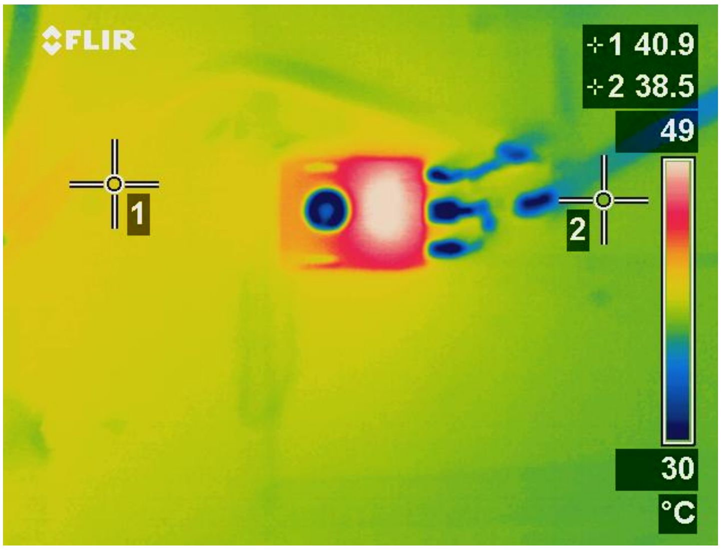

Figure 3.15: Experimental Temperature distribution of the diode 2 at P=10 W.

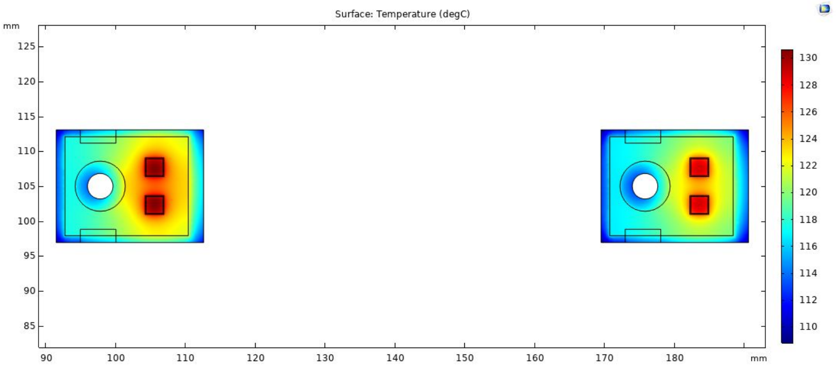

Figure 3.16: Temperature distribution at the junction for P=40 W.

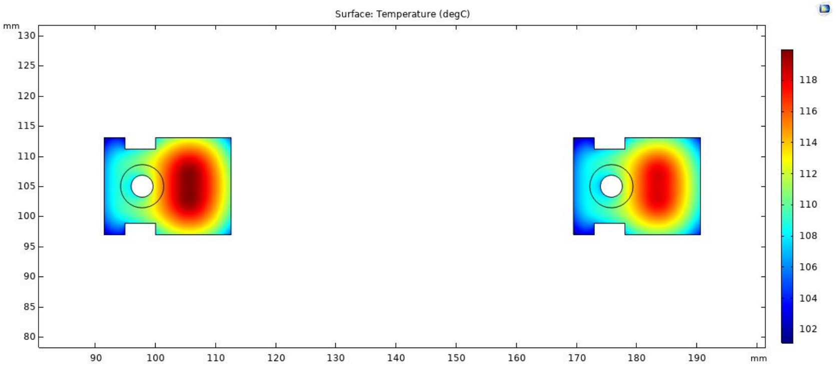

Figure 3.17: Temperature distribution of the top case of the diodes for P=40 W.

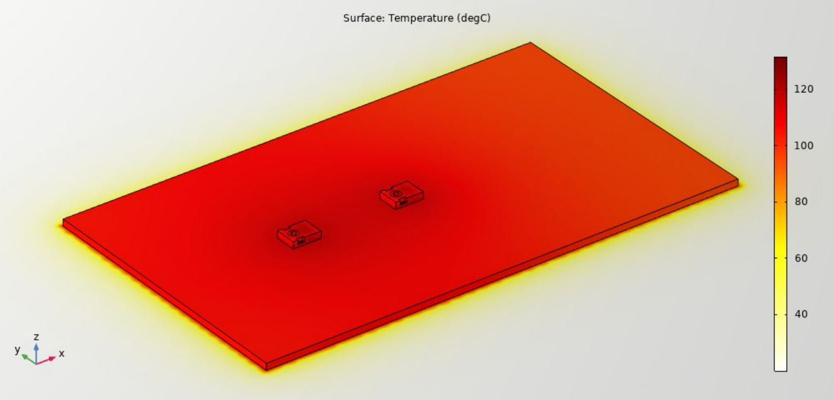

Figure 3.18: Temperature distribution the two diodes for P=40W.

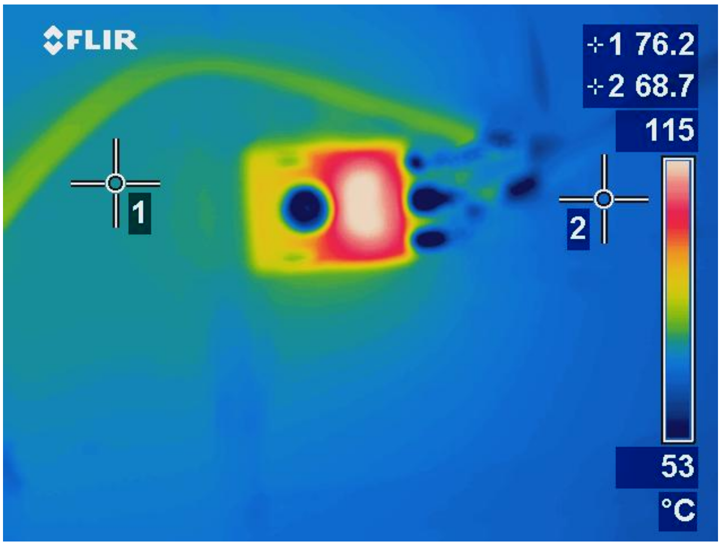

Figure 3.19: Experimental Temperature distribution of the diode 1 at P=40 W.

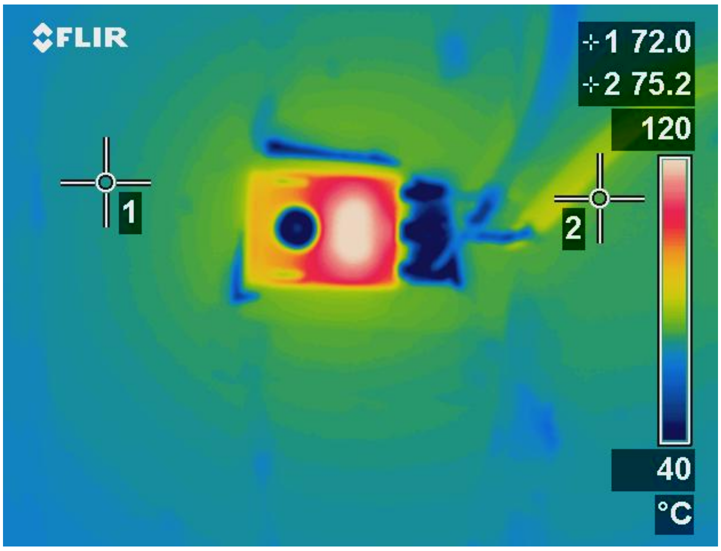

Figure 3.20: Experimental Temperature distribution of the diode 2 at P=40 W

Results Observation: The temperature distribution from the results obtained due to the simulation show great similarities when compared to the experimental results. One can notice that the simulation result in the Figure 3.11, when the power is increased to 10 W, the temperature rises to approximately to $50^{O}C$, this similar temperatures was also seen in the experiment when the power loss was increased from 0-10 W in the diodes from the set of Figure 3.14 and Figure 3.15. The similarities in temperatures both the cases concludes that heat flows mainly from the die chips to the copper frame below it to ensure that it flows finally to the aluminium plate for finally, the convection.

The experimental and the simulation results show similarities in the differences in the temperatures of the diodes. The diode 2, placed at the centre has lower temperature than diode 1 placed at the edge. This can be explained by the fact that the heat flows differently for both the diodes. The diode 2 is closed to $1^{o}C$ lower diode 1, as diode 2 is placed in the centre. It has more heat spread compared to the diode 1, as the diode 1 is closer to the edge.

The temperatures of the diodes during the experiment were slightly higher than the ones in simulation. This is due the property of the diodes where the temperature is dependent on the voltage. The layer of Polyimide placed below the diodes has proven to be an effective tool for heat transfer, through the experimental verification as it provides low thermal resistance and plugs all the air gaps between the interfaces of diode and the aluminum plate.

When the losses are increased to 40 W , as it can be seen from Figure 3.17, the heat flow increases. According to (3.2), the increase in heat flow increase the temperatures. Hence, we see temperatures of both the diodes going up to 120^oC. This is also experimentally verified from the set of Figure 3.19 and Figure 3.20. The temperature differences between the diodes this time even greater due to increased heat flow in the diodes.

Thermal Modelling of a rectifier

The simulation of the heat transfer model of two diodes in series and its experimental verification gives an insight into how heat flows in a system. The chip dies in two diodes produces losses due of which the heat is produced and moves through the copper frame to the aluminum plate. Then, the heat spreads across the aluminum plate and then to the wood and also due to convection. Now due to this, more complex cases can be explored like simulating a heat transfer model of a rectifier.

The rectifier is arranged in such a way that the diodes are equidistant from the edges of the aluminum plate to have same flow of heat and area of heat spread. The parameters for the arrangement of the diodes are as follows:

1. The distance between the length of the rectifier s:91mm
2. The distance between the diodes in each leg the rectifier d:28mm

The power losses are added to the diodes for P=10 W and 40 W. This is basically to observe the rise in temperatures in the system. The layers of Polyimide is placed between the surface contacts of all the four diodes and the Aluminum plate. Simulation of a rectifier would mean that there will be four heat sources as there are four diodes. Hence, the cumulative losses will be twice the previous case. The characteristic length of the aluminum plate, in this case, would be :

$$L_{AL} = \frac{Area}{Perimeter} = \frac{(l_{AL} \times h_{AL} - 4 \times E \times D)}{2 \times (l_{AL} + h_{AL})}$$

Therefore,

$$L_{AL} = 0.0651m$$

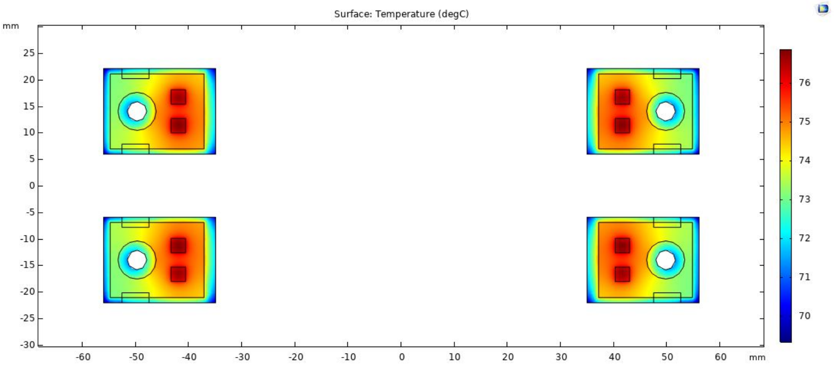

Figure 3.21: Temperature distribution of the junction of the diodes in the rectifier for P=10 W.

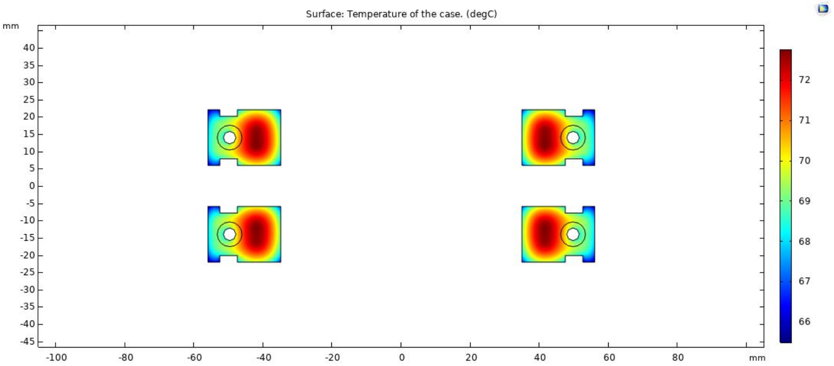

Figure 3.22: Temperature distribution of the top case of the diodes in the rectifier for P=10 W.

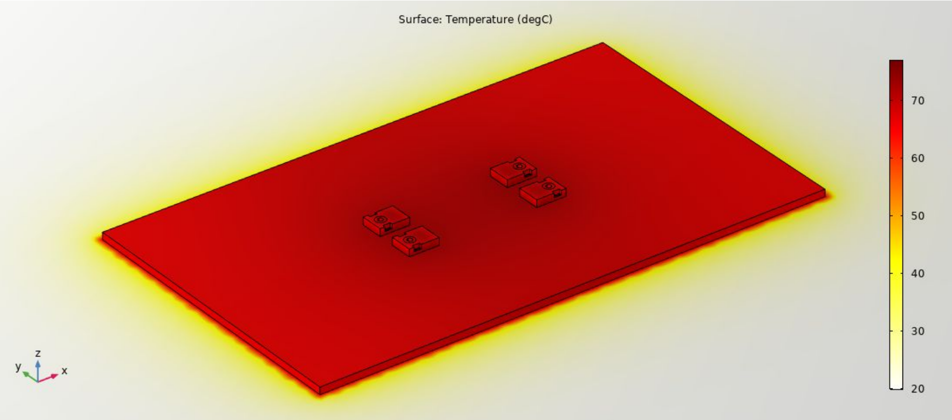

Figure 3.23: Temperature distribution of the rectifier for P=10 W.

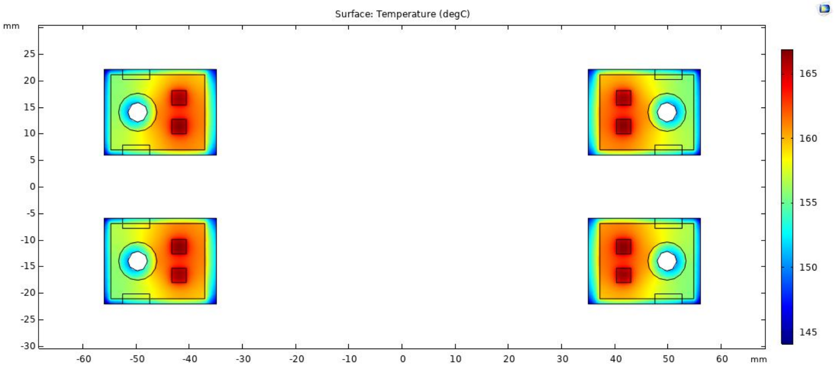

Figure 3.24: Temperature distribution of the junction of the diodes in the rectifier for P=40 W.

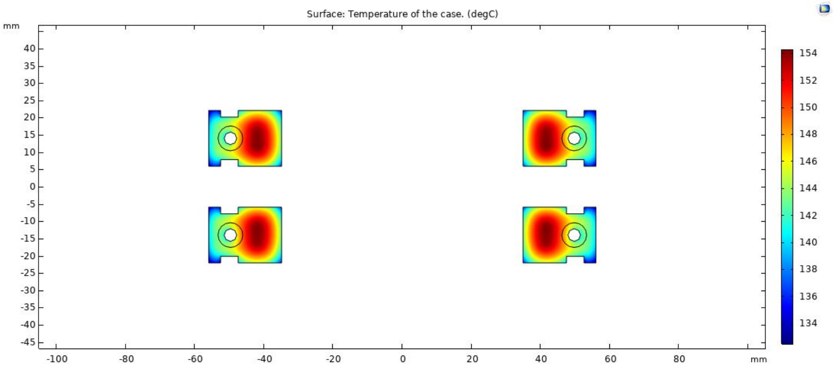

Figure 3.25: Temperature distribution of the top case of the diodes of the rectifier for P=40 W

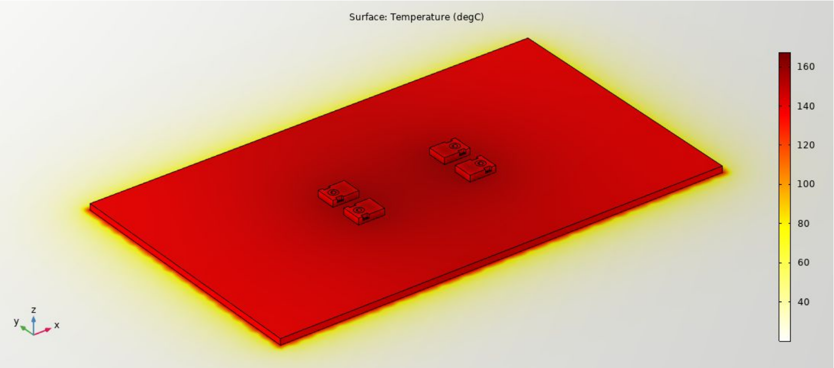

Figure 3.26: Temperature distribution of the Rectifier for P=40W.

Results Observation: The characteristic length of the aluminum plate is lower than in the previous case. The power losses are at to 10 W the temperatures rise up to 78^oC at the junction, unlike the previous experiment where at 10 W, the temperatures rise up to only 50^oC. The temperatures increases further as the power losses P=40W. This is due to, the presence of four heat sources hence, the heat flow increases and with a lower heat transfer coefficient the junction temperature will increase.

Selection of a heatsink

The heatsinks can play a crucial role in reducing the junction temperature of the diodes by improving their thermal performance [15]. In the simulation, the heatsink is placed on the aluminum pad which has the dimensions of the aluminum shield of the receiver. The length and breadth of the heatsink is varied by keeping one of the two dimensions fixed. The Junction and the Top case temperature were recorded for every case.

The proper selection of heatsink is done by placing the rectifier on the heatsink. The rectifier is arranged as described in the previous section. The losses applied on the diodes are P= 7.5 W. The dimensions of the heatsink are varied from the minimum i.e. dimensions equal to that of the arrangement of the diodes, to the maximum i.e the dimensions of the aluminum pad. The condition is to ensure that the top case of the diodes stay at the maximum temperatures of around 50^OC.

Understanding how heat flows in a heatsink is essential in getting an accurate heat transfer coefficient.The characteristic length of the heatsink L_{hs} is:

$$L_{hs} = \frac{l_{hs} \times w_{hs} - 4 \times E \times D}{2 \times (l_{hs} + w_{hs})}$$

where:

- The length of the heatsink=l_{hs};
- The width of the heatsink= w_{hs}.
- The thickness of the heatsink=t_{hs}=5 mm.

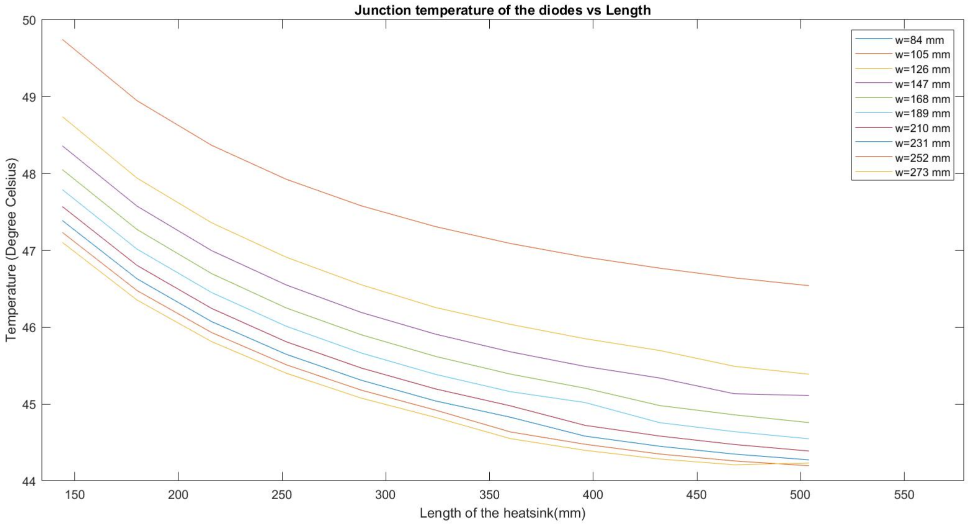

Figure 3.27: T_j vs Length

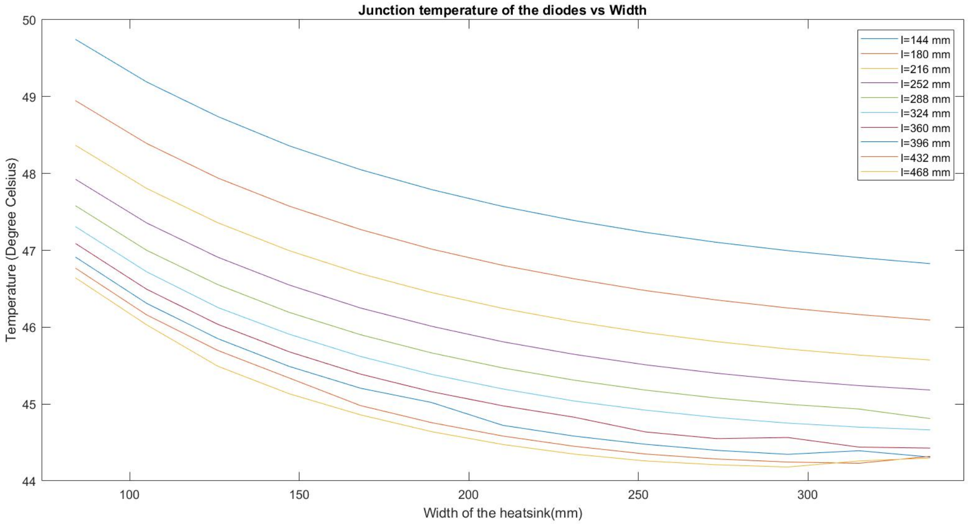

Figure 3.28: T_j vs Breadth

Results Observation: The results were plotted using values obtained from the COMSOL by varying the length and breadth of the heatsink.According to the graphs in Figure 3.27 as the length increases by keeping the breadth constant for each curve, the junction temperature decreases till a point it saturates. Just like that, the trend is same when the breadth of the heatsink increases like in the Figure (3.28). The junction temperature decreases with increases breadth also. Along the vertical axis, as we go down the space between the curves starts to shrink. Hence, the suitable way to pick the heatsink dimension is to select the saturation point as there is no further drop in temperature and increasing the dimensions could increase the weight of the entire system hence more energy consumed by the EVs, therefore the constraint of volume and bulkiness is addressed.From the graphs, one can observe that as the dimensions increase, junction temperature decreases. When either the length or breadth is increased, the area also increases which means the thermal resistance decreases. This leads to an increase in heat transfer coefficient, and as a result, the junction temperature decreases.

Modelling of the coil losses of the receiver pad

The next step is to analyze how the heat flows in the receiver pad when the current gets induced in the Litz wire. For this experiment, a DC current flows through the Litz wire to generate the losses produced due to current. The losses generate heat in the wire. The flow of generated heat is analyzed to observe the temperature distribution of the receiver pad. The structure of the receiver pad is designed in the set of figures depicted in the Figure 3.8, where the layers and the dimensions of the receiver coil are shown. To model the coil, the first step is to identify the losses generated in the litz wire, which would be the heat source. The used litz wire has the following features:

- Radius of the Litz wire r:1.25mm.
- Radius of the strands in the Litz wire r_s=0.0355 mm.
- material of the strand: Copper.
- material of the insulation: Epoxy mold.
- length of the entire litz wire L =16.79 m.
- number of turns N=20.

The features of the entire Litz layer are defined as follows:

- length of the Litz layer l_{Litz}=545mm.
- length of the air gap l_{ag}=245mm.
- breadth of the Litz layer b_{Litz}=350mm.
- breadth of the air gap b_{ag}=50mm.
- thickness of the Litz layer t_{Litz}= 2.5 mm.

The materials properties of the layers are given as follows:

- the density of the copper d_{Cu}=8920 kg/m^3;
- the density of the litz wire insulator (epoxy mold) d_i=1780 kg/m^3;
- thermal conductivity of the copper k_{Cu}=385 $W/(m.K)$;
- thermal conductivity of the insulator k_i=1.25 $W/(m.K)$.

To model an entire layer of Litz wire can be a difficult task. It is laborious to design the coil with turn after turn, as it will create lots of meshes as it leads to higher computational capacity. To simplify the modeling of the Litz wire, the solution is to combine both the coil and the surrounding air into one domain or a layer. And calculate the parameters like thermal conductivity, density, and heat capacity by taking the volumetric averages of both the materials Litz and the air [16].

The density of the material can be found by the calculating individual volumes and masses of the Litz and air. The volume of Litz wire is

$$V_{litz} = \pi \times r^2 \times L \tag{3.9}$$

$$V_{litz} = 0.8205cm^3$$

Hence, the mass of the Litz wire is:

$$m_{Litz} = V_{Litz} \times d_{Litz} \tag{3.10}$$

where d_{Litz} is the density of the Litz wire. To calculate the density of the Litz wire, the material consists of copper and epoxy mold:

$$d_{litz} = \frac{m_{cu} + m_i}{V_{cu} + V_i} = \frac{V_{cu} \times d_{cu} + V_i \times d_i}{V_{cu} + V_i} \tag{3.11}$$

$$V_{cu} = (2.3/0.071) * pi * (0.071e - 3)^2 * L/4 = 0.021cm^3$$

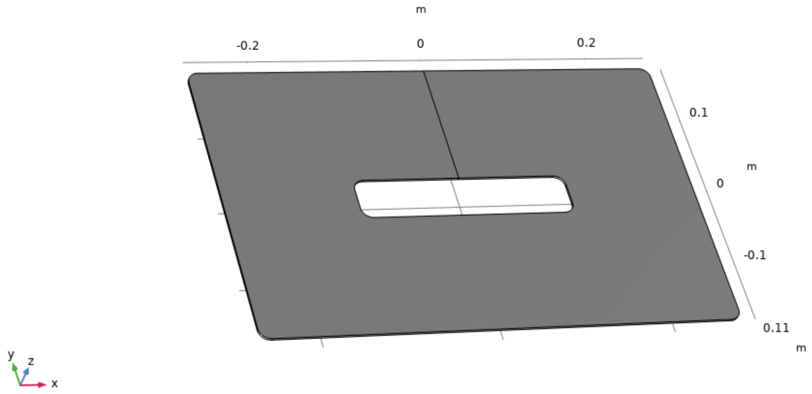

Figure 3.29: The Litz layer of the coil to be modelled as a domain.

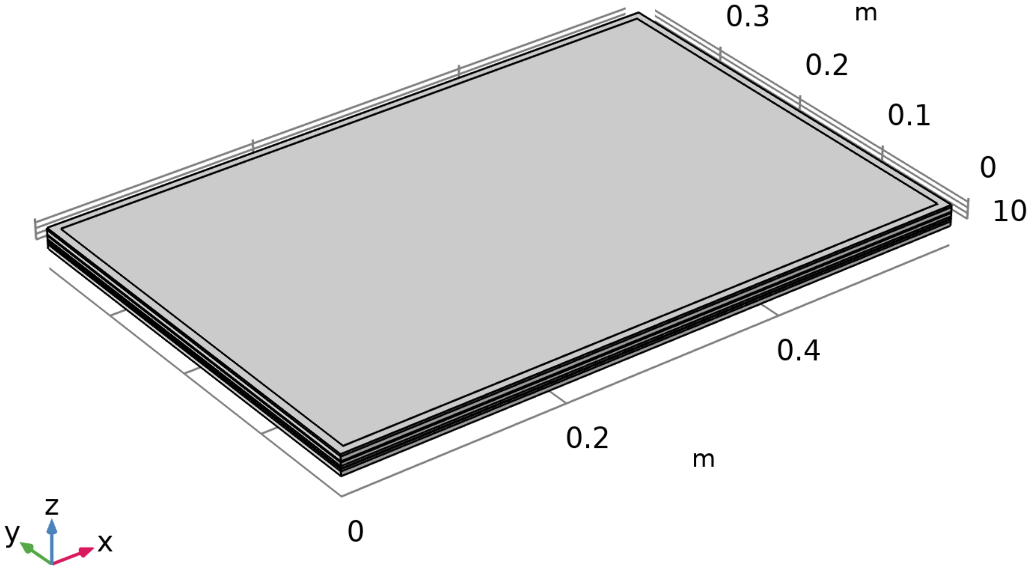

Figure 3.30: The reciever pad designed on COMSOL.

The volume of the insulation in the Litz wire is:

$$V_i = V_{Litz} - V_{coil} = 0.803 cm^3$$

Hence, the density of the Litz wire is:

$$d_{Litz} = 1966.66 kg/m^3$$

So, the mass of air in the layer can be calculated from the ratio between the volume of air and the density of air:

$$V_{layer} = l_{Litz} \times b_{Litz} \times t_{Litz} \tag{3.12}$$

The volume of the entire litz layer is:

$$V_{layer} = 4.77cm^3$$

The mass of the Litz wire is:

$$m_{Litz} = V_{Litz} * d_{Litz} = 0.1621Kg$$

Therefore, the volume of air is:

$$V_{air} = V_{layer} - V_{Litz} \tag{3.13}$$

$$V_{air} = 3.94cm^3$$

and the mass of the air in the layer is:

$$m_{air} = V_{air} \times d_{air} \tag{3.14}$$

The mass of the air in the coil is:

$$m_{air} = 0.48kg$$

Therefore, the density of the entire mixed layer is:

$$V_{layer} = \frac{m_{Litz} * d_{Litz} + m_{air} * V_{air}}{V_{layer}} = 1361.9kg/m^3 \tag{3.15}$$

The heat capacity of the litz layer $C_{p,layer}$ is calculated by:

$$C_{p,layer} = \frac{m_{air}}{m_{air} + m_{Litz}} C_{p,air} + \frac{m_{Litz}}{m_{air} + m_{Litz}} C_{p,Litz} \tag{3.16}$$

where, $C_{p,air}$ and $C_{p,Litz}$ are the heat capacities of air and litz respectively. Hence, the heat capacity of the layer is:

$$C_{p,layer} = 848.51J/K$$

The calculation of the thermal conductivity of two combined materials needs a proper understanding of how heat flows in the receiver. The thermal conductivity of most materials is assumed to be isotropic, i.e., the quantity doesn't change in all directions. In this case, the thermal conductivity of the material is going to be different in all directions. But when there is a presence of a ferrite layer and aluminum sheet. These layers are good conductors of heat, they offer less thermal resistance. Hence, most of the heat flows in the vertical direction from bottom to top as the metal layers will provide low thermal resistance to the heat transfers. The thermal resistance of the Litz wire can be calculated by:

$$R_{Litz} = \frac{t_{Litz}}{k_{Litz} \times A_{wire}} = 9.02^oC/W$$

where the thickness of the Litz layer, t_{Litz} is the thickness in the direction of the heat flow. Whereas, the area of the Litz wire is the area of cross section perpendicular to the flow of heat.

$$A_{wire} = 2\pi \times r \times L$$

and the thermal conductivity of the Litz wire k_{litz} can be found out by [17]:

$$k_{Litz} = k_i \frac{(1 + V_C)k_C + (1 - V_C)k_i}{(1 - V_C)k_C + (1 + V_C)k_i} = 1.32W/m.K$$

k is the equivalent thermal conductivity of the material, V is the volumetric contribution of the individual materials. The subscripts C and i indicate conductor and insulator, respectively. And just like that, the thermal resistance of the air in the coil is:

$$R_{air} = \frac{t_{Litz}}{k_{air} \times A_{air}}$$

where area of cross section of air is:

$$A_{air} = A_{layer} - A_{wire}$$

Hence, the thermal resistance of air is:

$$R_{air} = 134.6904^{o}C/W$$

The area of the cross section of air is:

$$A_{air} = 678.65cm^{2}$$

As they are two different materials, the thermal resistances are in parallel. Hence, the net thermal resistance of the layer R_{layer} is :

$$R_{layer} = \frac{R_{Litz} \times R_{air}}{(R_{Litz} + R_{air})}$$

$$R_{layer} = 8.9127^{o}C/W$$

Then, the thermal conductivity of the layer of the combined materials of the wire and air is:

$$k_{mat} = \frac{t_{Litz}}{(R_{Litz} \times A_{layer})}$$

Therefore, the net thermal conductivity of the layer is:

$$k_{mat} = 0.3167W/m.K$$

After the main parameters necessary for the simulation have been calculated the next step is to calculate the heat transfer coefficient. As the heat flows from top to bottom, it is safe to say the receiver pad can be modeled as a vertical wall [18].

$$h = \begin{cases} \frac{k}{L}\left(0.68 + \frac{0.67Ra_L^{\frac{1}{4}}}{\left(1+\left(\frac{0.492k}{\mu C_P}\right)^{\frac{9}{16}}\right)^{\frac{4}{9}}}\right) & \text{if} Ra_L \leq 10^{9} \\ \frac{k}{L}\left(0.68 + \frac{0.67Ra_L^{\frac{1}{4}}}{\left(1+\left(\frac{0.492k}{\mu C_P}\right)^{\frac{9}{16}}\right)^{\frac{4}{9}}}\right) & \text{if} Ra_L > 10^{9} \end{cases} \tag{3.17}$$

where L is the height of the wall, i.e., the thickness of the receiver pad.

$$L = 26.7mm$$

If the density depends only on the temperature.The Rayleigh' s number is defined as:

$$Ra_L = \frac{g\alpha_P \rho^{2} C_P |T - T_{ext}| L^{3}}{k\mu} \tag{3.18}$$

If not, then it depends on other parameters:

$$Ra_L = \frac{g\rho C_P |\rho - \rho_{ext}| L^{3}}{k\mu} \tag{3.19}$$

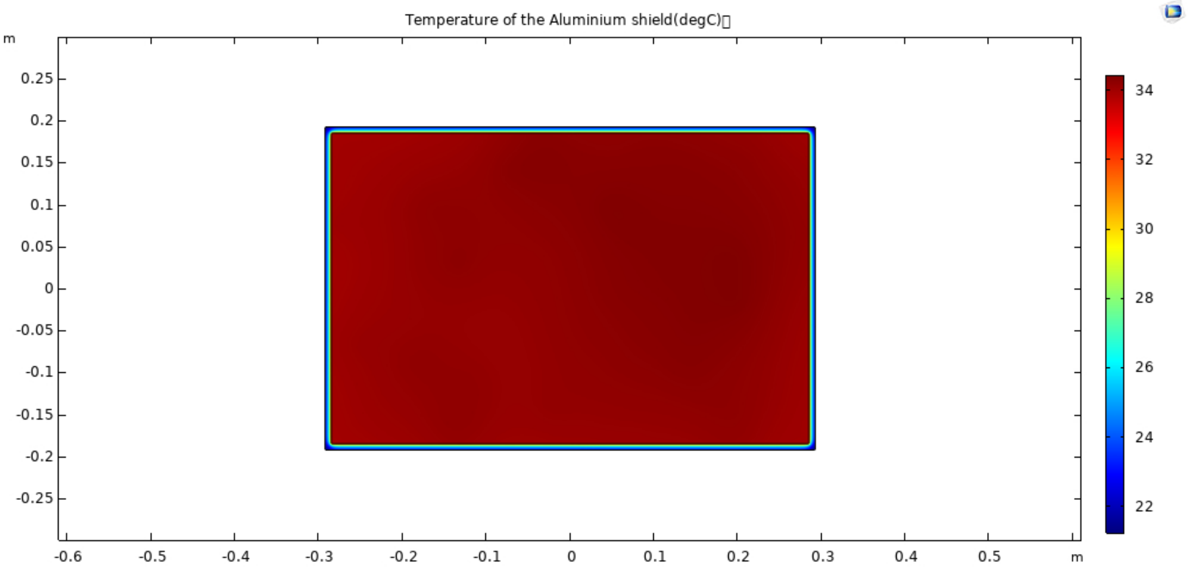

Figure 3.31: The reciever pad designed in COMSOL.

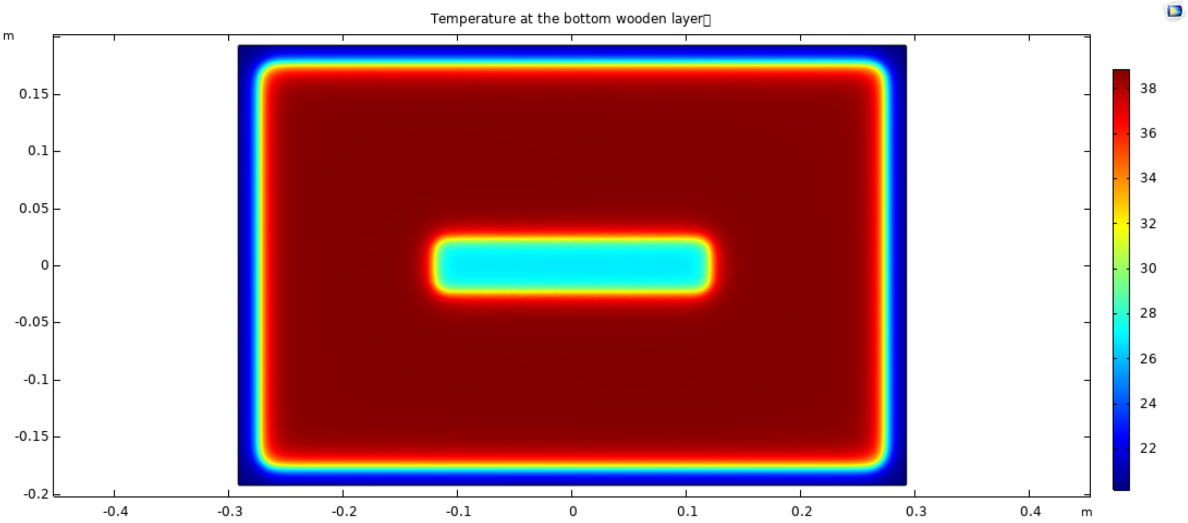

Figure 3.32: The reciever pad designed in COMSOL.

Results Observation: From the simulation, it is understood that when the coil is placed inside the receiver pad at the bottom, there is a temperature gradient from the bottom to the top. The highest temperature is at the coil where the heat is produced and as we move to the top, the temperature reduces. The heat flows mainly in two ways. One is from the coil to the wooden layer below, and the other is from the coil to the topmost of the aluminum shield. The temperature at the bottom is higher than the temperature at the top, as the thermal resistance from the coil to the aluminum shield is lower than the thermal resistance from the coil to the bottom wooden layer. The temperature distribution at the Figure 3.32, has shown that there is a temperature variation across the Litz layer. The lowest temperatures are at the air gap in the middle. This is due, the air being a bad conductor of heat and can offer high thermal resistance. The highest temperature is in the litz wire as the wire is main source of heat in the receiver pad.

3.2.1. Cooling the diode bridge on the reciever pad with a heatsink vs without a heatsink

The constraint of weight is also an important factor in modelling of the receiver pad. In the previous sections of this chapter, the dimensions and the arrangement of the heatsink has been discussed for the four diodes. That heatsink would be placed on top of the aluminium shield of the receiver coil, with a thermal interface material in between. Another option would be to increase the thickness of the aluminum shield and attach the diodes directly there. However, this would influence the total weight of the receiver pad. The possible weights of the receiver pad are shown in Table 3.4 and 3.5 for the case without a heatsink and the one with the heatsink, respectively.

Thickness of Aluminium shield	Weight(Kg)	Junction temperature(^oC)
2mm	4.38	55.5
3mm	4.96	50.9
4mm	5.54	50.8
5mm	6.11	49.8
6mm	6.69	49.2
7mm	7.27	48.6

Table 3.4: Weights for receiver pad when no heatsink is used

Thickness of Heatsink	Weight(Kg)	Junction temperature(^oC)
5mm	4.82	50.74
6mm	4.90	50.45
7mm	4.99	50.25
8mm	5.08	50.01
9mm	5.16	49.81
10mm	5.25	49.80

Table 3.5: Weights for receiver pad when heatsink is used with Aluminium shield thickness t_{AL}=2mm

Results Observation: The weights of the receiver pad and the junction temperatures of was and every case of thickness was recorded. From the table 3.4, increasing the thickness can reduce the junction temperatures of the diodes but increase the overall weight of the system. From the table 3.5, increasing the thickness of the heatsink reduces the junction temperature, but the overall weight of the system is not as high as the previous case. It is recommended to chose a heatsink with the thickness of 5mm, with thickness of aluminium shield of 2mm.

3.2.2. Observations

From the following steps for the experimental verification to achieve the final goal following conclusions were deduced:

- With the increase in Aluminium shield thickness, the thermal resistance decreases which results in a decrease in the junction temperature.
- With increase in area of Heatsink dimensions the junction temperature decreases due to decrease in thermal resistance.
- The increase in thickness adds to the bulkiness of the prototype. Hence t_{AL}=>2mm can show lower junction temperatures without the heatsink.
- Hence it is recommended that using the heat sink dimension of l=0.216 m and w=0.147 m with the aluminium shield thickness of 2mm.
- s=91mm and d=28mm would be the right recommended dimensions for the arrangement of the diodes as there is no significant decrease in temperature with minimal changes in the dimensions of diode arrangement.

4

Experimental verification

The final step of this research is the thermal analysis of the total system, where the rectifier with a heatsink is placed on a receiver pad such that the constraints of bulkiness, compactness and thermal management can be solved. The rectifier is placed in the middle of the aluminum shield so that the heat flows are equal for all four diodes. It is preferable to place the rectifier in the middle of the aluminum shield as it's the coolest place across the entire shield. There are two sources of heat generated in the system. As we know, one is the rectifier-diode bridge and the second is due to the current flowing through the litz wire. With the presence of more heat sources, the junction temperatures of the diodes will go up and so will the temperature of the coil. The heat produced from the diodes not only spreads throughout the heatsink but also flows to the aluminum shield and spreads throughout it.

The individual thermal modeling of the receiver and the rectifier gave an understanding of how heat flows in both cases. For a rectifier, the heat mainly flows from the chip to the lead frame, and then to the heatsink. The heat spreads throughout the heatsink and then finally convection happens where the heat transfers from the heatsink to the air. Similarly, in the case of the receiver winding, the heat flows from the coil to both the aluminum shield and the wooden layer below it.

4.1. Simulation of the full system

The simulation of the entire system gives an idea of how the system must perform in a given environment. The results of this simulation are crucial in understanding how accurate the model is when compared to the experiment. This could help one in realizing the differences in the results for generating a better model in the future. The geometry of the entire system is shown in Figure 4.1.

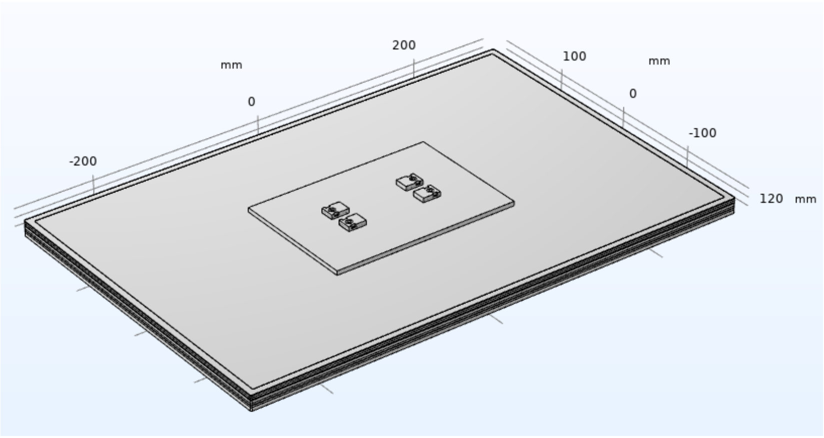

Figure 4.1: The reciever pad experimental.

4.1.1. Thermal Interface Materials (TIM)

There are two places where thermal interface materials are used to have a smooth transfer of heat:

- the thermal pad made of Polyimide is used underneath the diodes for the transfer of heat from the chips to the heatsink;

- the thermal paste made of Dimethylsiloxane used underneath the heatsink for the transfer of heat from the heatsink to the aluminium shield.

The features of both the thermal layers are listed in Table 4.1.

Product name	DOW CORNING 340	BERGQUIST SIL PAD TSP K1300
Material	Dimethylsiloxane	Polyimide
Location	Underneath the diodes	Underneath the heatsink
Thickness	$50\mu m$	0.15mm
Heat capacity	1460 J/(kg.K)	1100 J/(kg.K)
Density	970 kg/m^3	1300 kg/m^3
Thermal conductivity	1.3(W/m.K)	0.15(W/m.K)

Table 4.1: Material properties of thermal pads

The thermal resistance per unit of area of the these TIMs are:

$$R_{th,PI} = 0.2 \circ Cin^2/W = 0.000129032 \circ Cm^2/W$$

and

$$R_{th,hs} = 0.16 \circ Ccm^2/W = 0.000016 \circ Cm^2/W$$

where $R_{th,PI}$ and $R_{th,hs}$ are thermal resistances in a unit area of BERGQUIST SIL PAD TSP K1300 and DOW CORNING 340 respectively. Hence, the net thermal resistances provided due these TIMs are:

$$R_{PI} = 0.000129032 \circ Cm^2/W \times (Area)_{Diode} = 4.39 \times 10^{-8} \circ C/W$$

and

$$R_{hs} = 0.000016^o Cm^2/W \times (Area)_{PI} = 5.08 \times 10^{-8} \circ C/W$$

where R_{PI} and R_{hs} are thermal resistances of BERGQUIST SIL PAD TSP K1300 and DOW CORNING 340 respectively.

4.1.2. Simulation Results

The simulation is conducted to get an understanding of thermal management of the system which could be useful result during practical environment. The results of the full system are shown in the set of Figures from (4.2) - (4.8). During the previous simulations where the rectifier and the receiver pad were modeled separately. It can be seen in Figures (4.2) (4.3) and (4.4) the temperatures are higher when the entire system is simulated. This is due to the presence of more heat sources in the system so the flow of heat increases. The temperature of the bottom wooden increases to 38^oC, while the temperatures of the top case of the diode increase up to 49^oC.

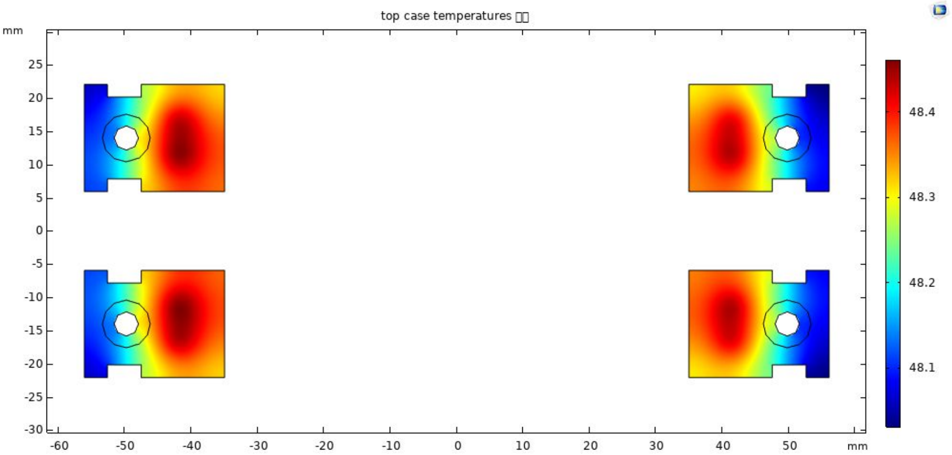

Figure 4.2: Thermal distribution of top case of the diodes.

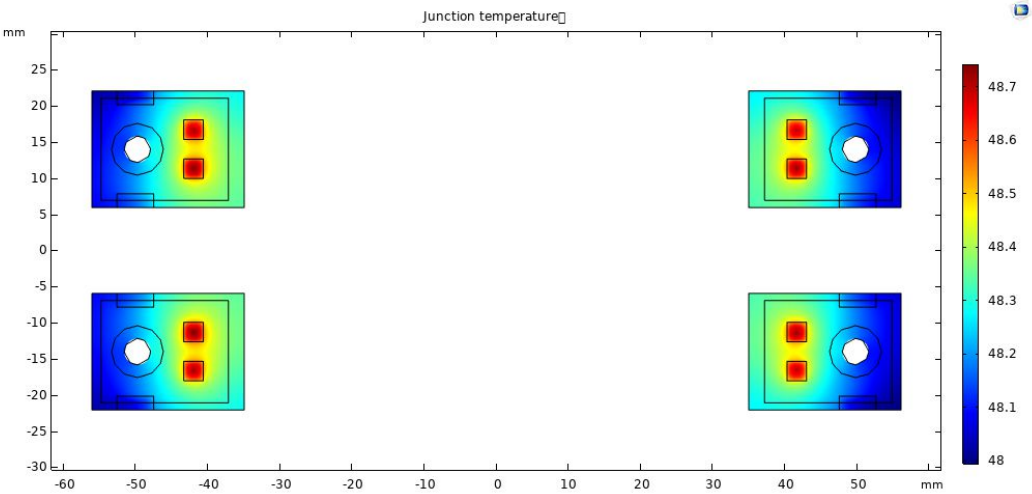

Figure 4.3: Thermal distribution of chip of the diodes.

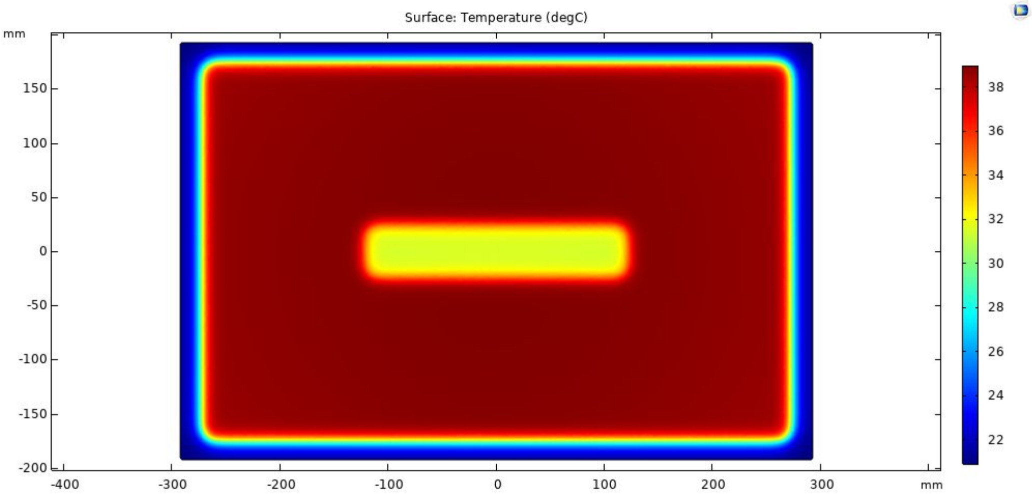

Figure 4.4: Thermal distribution of bottom wooden layer.

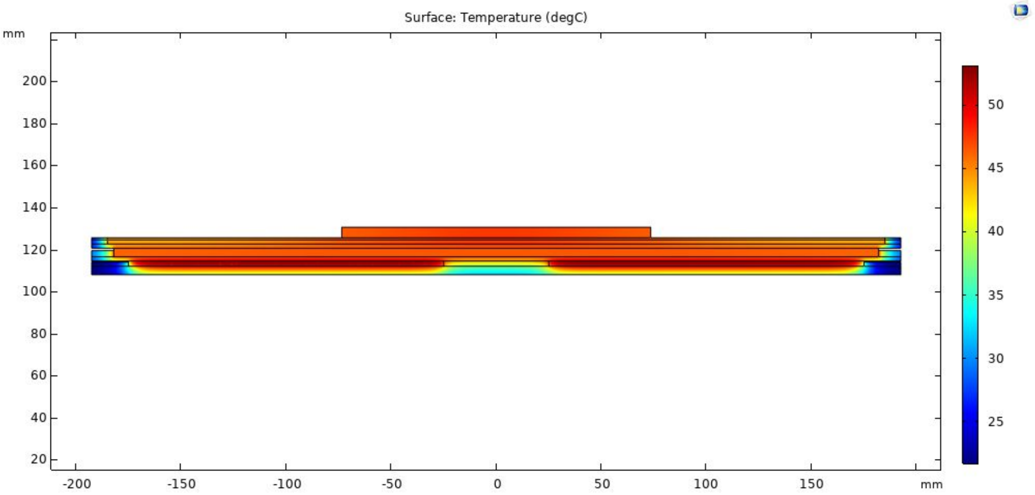

Figure 4.5: Thermal distribution of different layers in the reciever.

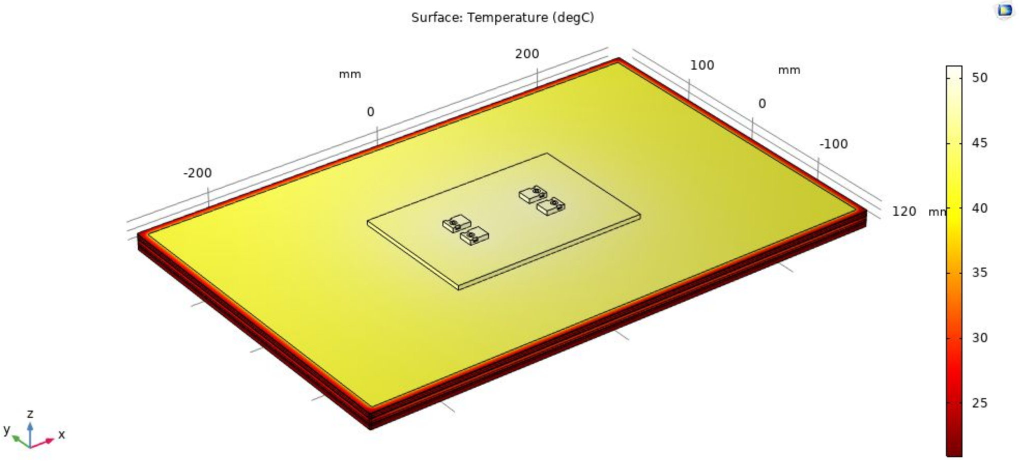

Figure 4.6: Thermal distribution of the reciever.

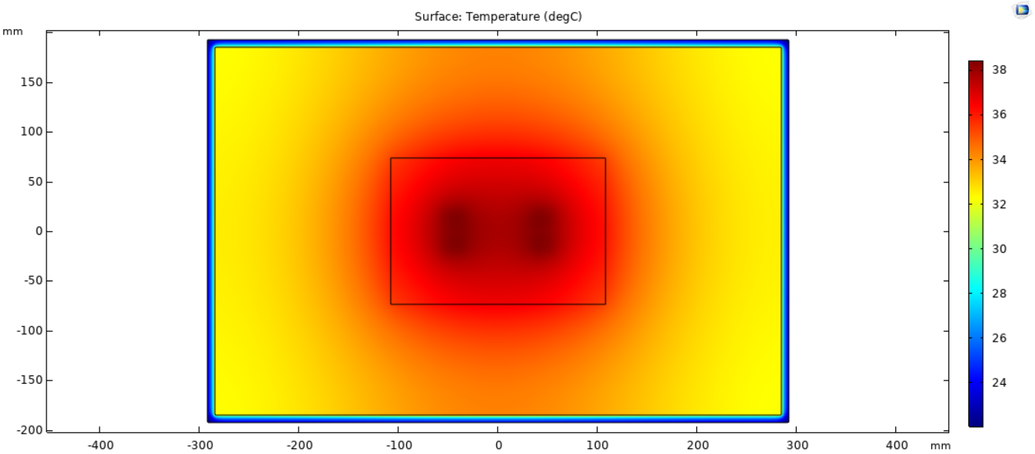

Figure 4.7: Thermal distribution of the Aluminum shield.

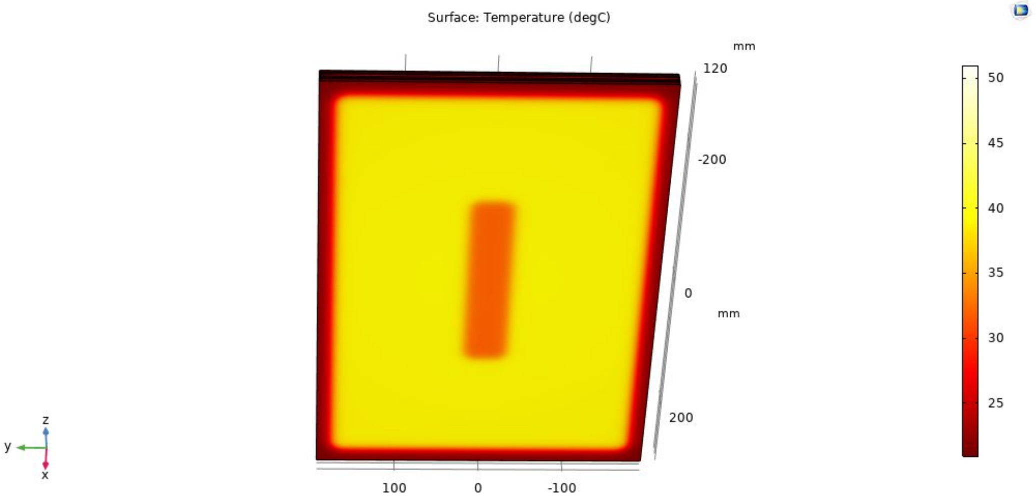

Figure 4.8: Thermal distribution of the bottom of the reciever.

4.2. Experimental result

The experiment was conducted to ensure whether the results in the simulation of the thermal model were accurate or not. Figure 4.9 shows the setup of the experiment of the receiver pad. The diodes are connected in series through solder on a breadboard. There are two DC power sources connected to the setup: one is the power source connected to the coil and the other is the power source connected to the four diodes. To verify the simulated results, the two sources supply DC power instead of the nominal high-frequency AC power. This choice make it easier and safer to run the prototype for a long time without the risk of being exposed to potentially dangerous magnetic fields. The aluminum shield and the heatsink are entirely covered in tape as the surface of the aluminum has a high reflectivity which would reflect the light and it would not be possible to measure the temperature with the thermal camera.

The set of figures from Figure 4.10 to Figure 4.12 were recorded over a period of time as diodes are active components, and the devices in the system take time to achieve the steady-steady temperature. The top temperatures of diodes and the coil are recorded with respect to time in Table 4.2 and Table 4.3, respectively. The room temperature recorded was recorded to be 20.9°C.

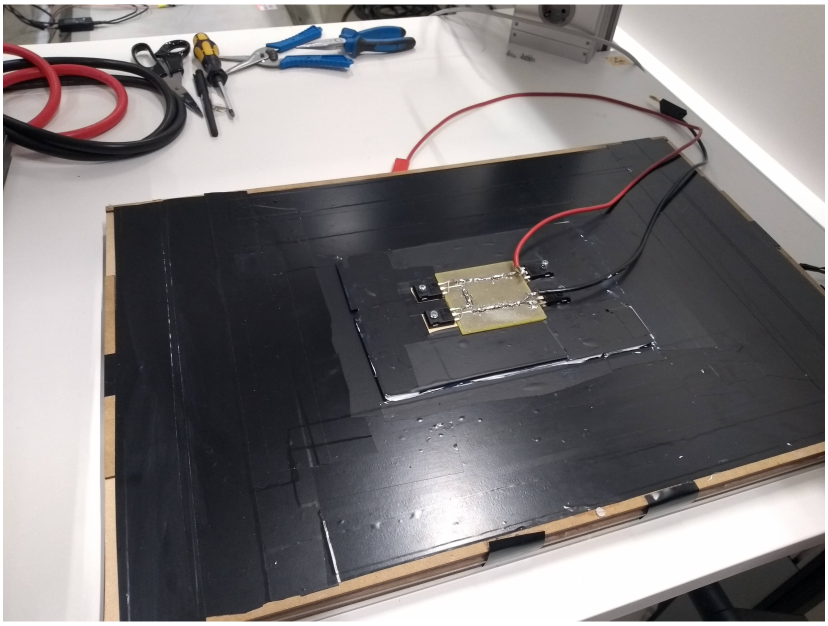

Figure 4.9: The reciever pad experimental.

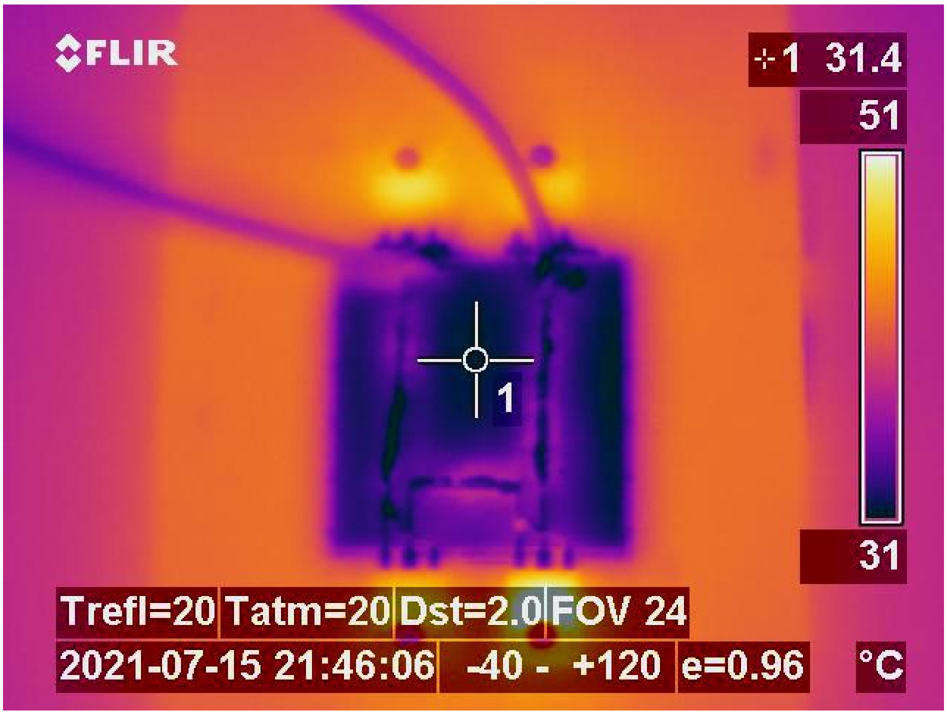

Figure 4.10: Temperature of the top case of the diodes at 11:16 am.

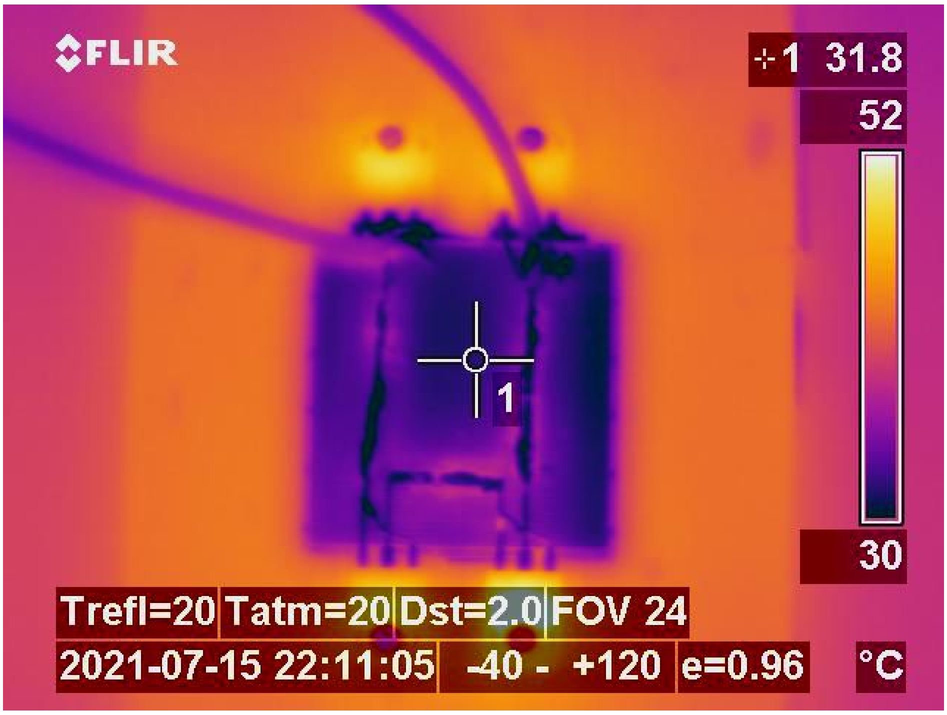

Figure 4.11: Temperature of the top case of the diodes at 12:20 pm.

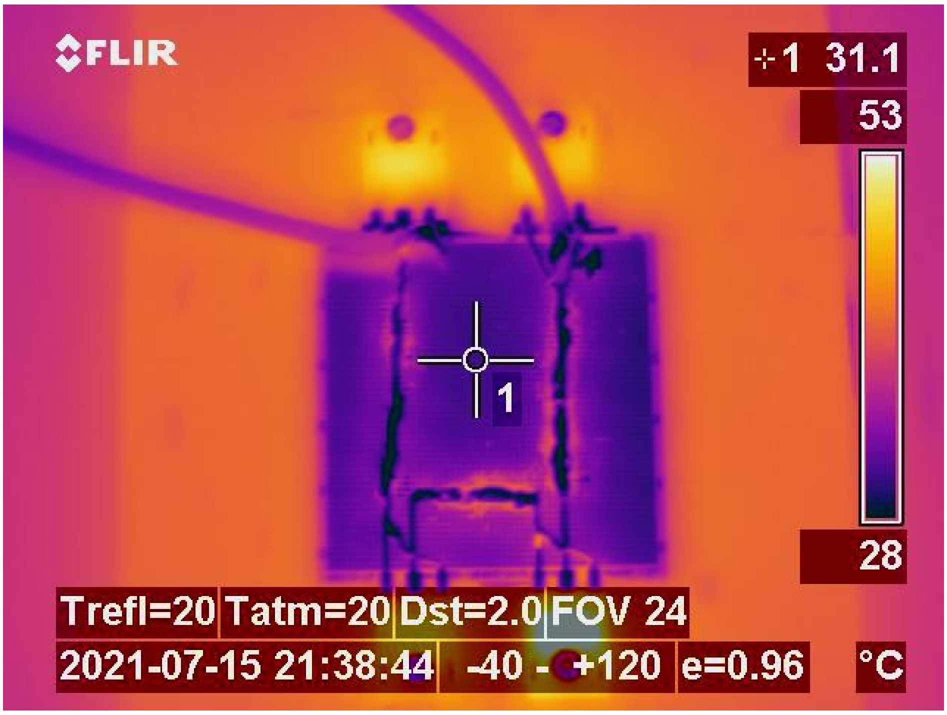

Figure 4.12: Temperature of the top case of the diodes at 12:50 pm.

Table 4.2: Temperature of the diodes over time

Time	Voltage(V)	Current(A)	Power loss (W)	Top case Temperature (T_t in degC)
10:21	0	0	0	0
10:35	4.9	6	30	30
10:56	4.9	6	30	39
11:16	4.9	6	30	50
11:57	4.9	6	30	52
12:50	4.9	6	30	53
13:50	4.9	6	30	54

Table 4.3: Temperature of the coil over time

Time	Voltage(V)	Current(A)	Power loss (W)	Temperature of the bottom wooden layer (degC)
10:21	0	0	0	20.9
10:35	2.9	14.1	40.89	20.2
10:56	3.0	14.1	42.30	25.2
11:16	3.0	14.1	42.30	29.2
11:57	3.1	14.1	43.71	34.0
12:20	3.1	14.1	43.71	36.0
12:50	3.1	14.1	43.71	38.2
13:20	3.1	14.1	43.71	38.5
13:50	3.2	14.1	45.72	39.4

4.2.1. Observations

The experiment was conducted over about 4 hours to record the steady-state temperatures. The diodes have a combined power loss of 30 W, and as they are all the same model, then each diode has a power loss of 7.5W. The losses in the diodes and the coil generate heat flow in the system and this creates a temperature gradient over the period. Compared to the simulation there are following difference.

- The top case temperatures of the diodes in the simulation and the experiment have some variation in the temperatures. This is since the paste used for the heatsink was not uniformly applied. This creates air gaps between the heatsink and the aluminum, which generates an additional thermal resistance of air as it impacts the heat transfer. Overall, the temperature difference between the simulation and experiment is around 2-4 percent.

- The junction temperature of the diode is dependent on the voltage of the power supply. As temperature increases, the voltage increases, which results in slightly higher power losses.

- The temperature in the bottom wooden layer is almost similar in the simulation experiment. The temperature increases to approximately 38.5°C due to the presence of more heat sources. The heat produced by the coil also flows through the heatsink which results in higher temperatures.

- The layers on the receiver will have slightly higher temperatures due to the presence of rough surfaces between them. The air gaps create thermal capacitance, which results in an increase of temperature.

5

Thermal Circuit

The thermal circuit is basically an equivalent circuit which mathematically shows the temperature distribution and the flow of heat across the system. In this thesis, the thermal model is drawn forthe lump of the receiver pad and the power electronics. The thermal circuit has basic analogies to the electrical circuits. These analogies is described in Table 5.1.

Table 5.1: Thermal Analogy

Electrical circuit	**Thermal Circuit**
Resistance	Thermal Resistance
Capacitance	Thermal Capacitance
Voltage	Temperature
Current	Power loss

To design the thermal circuit of entire system, it can be divided into two halves: one for the power electronics and other one for the receiver pad. The diodes of the rectifier are attached on a heatsink with the layer of Polyimide to facilitate an effective heat transfer. The net power loss of the Rectifier is:

$$P_{loss} = 4 \times 7.5W = 30W$$

The simulations in COMSOL of the power electronics mounted on the heatsink shown in Figure 5.1 have shown the thermal distribution of Figure 5.2.

To calculate the thermal resistance of the heatsink:

$$T_j = (R_{hs} + R_{jc}) \times P_{loss} + T_{amb} \tag{5.1}$$

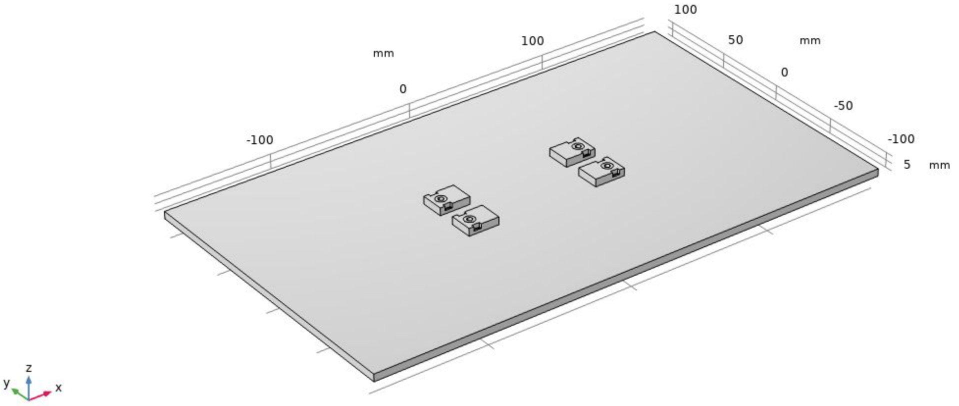

Figure 5.1: Geometry of the power electronics mounted on the heatsink.

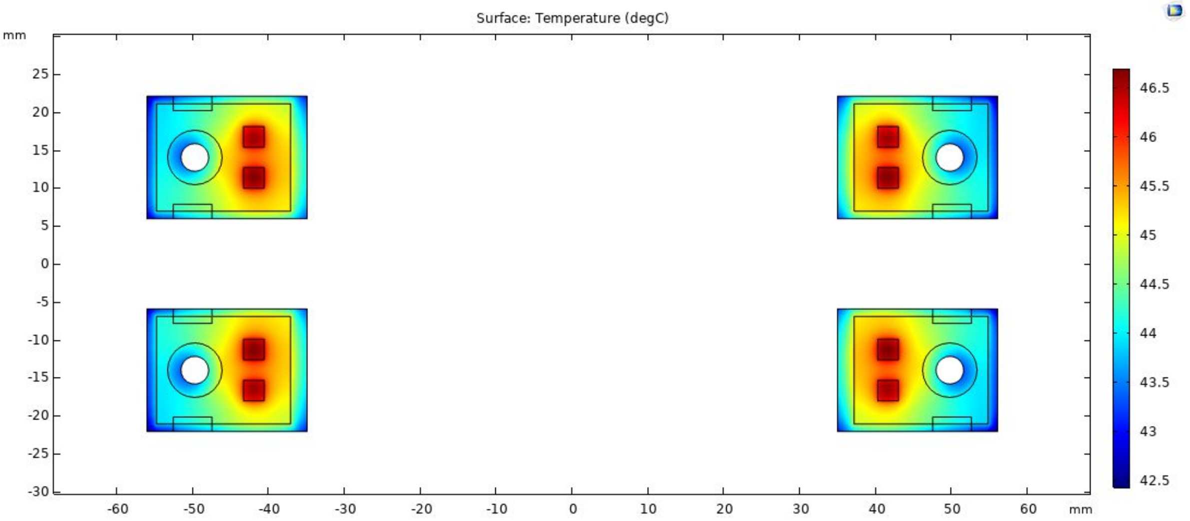

Figure 5.2: Junction temperature of the diodes from COMSOL

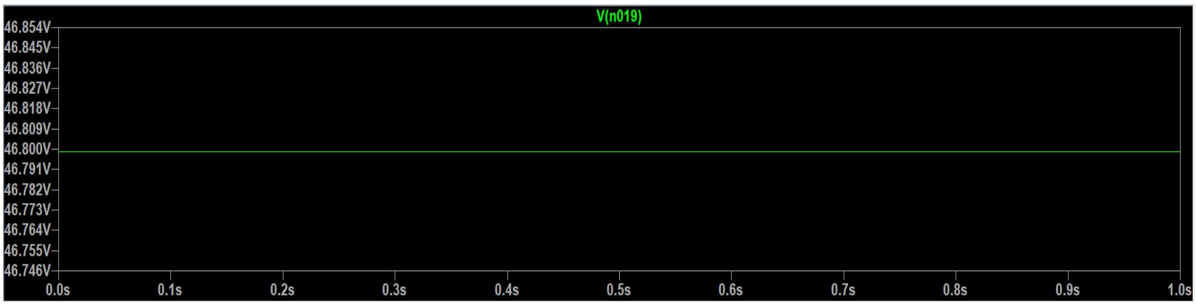

Figure 5.3: Junction temperature of the diodes from LT-SPICE

where:

- the junction temperature of the diode T_j=46.84°C;
- the ambient temperature T_{amb}=20.9°C;
- the power loss P_{loss}=30 W
- the thermal resistance from junction to the case R_{jc}=0.14°C/W
- R_{hs} is the thermal resistance of heatsink.

Hence using (5.1), the thermal resistance of the heatsink is:

$$R_{hs} = 0.72^{o}C/W$$

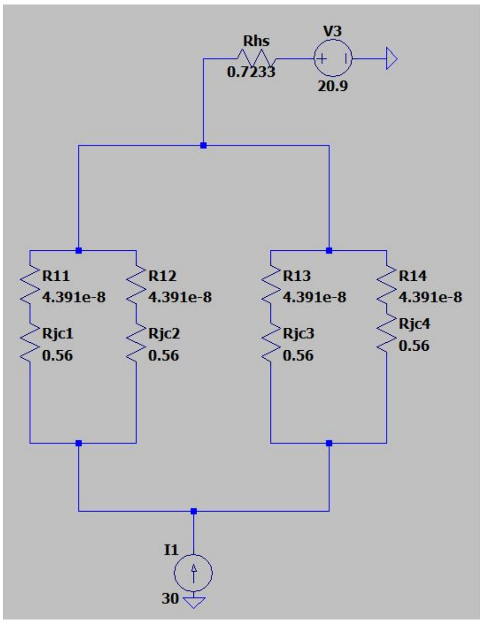

Figure 5.4: Thermal circuit of the rectifier

6

Conclusion

In recent years, there have been significant breakthroughs in the field of Wireless Power Transfer (WPT). Several models have been proposed over the recent years which provide an effective demonstration in a working environment. The effective utilization of the physical space has been a major roadblock to the development of electric vehicles (EVs), especially in WPTs. The receiver coil is placed under the vehicle chassis, and the power electronics also occupy some space. Hence, power density is a challenge. Due to the power operating level and frequency range, the thermal performance of these circuits is essential. The main goal of this thesis was to propose a model where placing the rectifier on top of the aluminum shield of the receiver pad can provide one flat solution where the constraints of space, power density, and weight are all sorted. In addition, a methodology for the selection of heatsink for the rectifier was proposed to improve its performance.

These objectives are achieved by modeling the rectifier and the receiver in the software environment of COMSOL 5.6a. The software models provide critical information on how the heat transfer impacts different components and layers across the system. This model can be used for different sizes of layers for ferrite and aluminum layers and other coil structures for the system. It can also be extended further to higher power levels for heavier vehicles.

The model has used rectangular planar (RP) as the preferred coil topology chosen for the working of the receiver pad. The RP performs better than most other pads as it has high efficiency and a low-leakage field.

To investigate the losses across different components in the WPT system, the equivalent circuit was designed on LT-Spice software and compared with MATLAB. The losses in the secondary system mainly come from the coil and the power electronics. The circuit's Operating frequency is at 85 kHz, and the passive components are operating in resonance to facilitate maximum power transfer and higher efficiency. The losses in the system are essential to the thermal analysis of the model as they are the sources of heat that create the temperature gradient from one point to another. The losses in the rectifier happen mainly due to conduction and switching in each diode over a period, which creates heat and increases the diodes' junction temperature of the diode. The losses were calculated at the worst-case scenario when the output voltage is at V_{out}=400 V so that the model designed is prepared for worst-case conditions.

The heatsink has proven to be an essential component in the thermal management of junction temperatures. The methodology devised for the selection and the graphs plotted for the dimensions of heatsink w.r.t the junction temperatures have shown the minimum dimensions needed for placing the power electronics on top of the heatsink. When compared to just using the aluminum pad as a heat spreader, the heatsink has played a better role as it provides lower junction temperatures and also makes the prototype of the receiver pad lighter. The designing and simulation of the coil have shown that the heat flows in the path of less thermal resistance. Hence from the results, it was shown that the heat flows from the coil to the aluminum shield and the bottom wooden layer, and is negligible in the other directions.

The practical experiment of the final prototype with the power electronics attached the heatsink has shown almost accurate values when compared to the simulation. Between the simulation and the experiment, there was a difference of 2-4% in the top case temperatures. The error is due to non-uniformity in the thickness in heatsink paste. Since the pressure applied on the heatsink was not enough, there were air gaps in the heatsink paste, due to which the heatsink paste was not so effective. The bottom of the receiver had similar temperatures in the simulation and the experiment. The losses in the experiment were higher due to the operation of the diodes: the forward voltage depends on the junction temperature. Hence, the losses would become higher which results in higher temperatures. The surfaces between different layers of the receiver play a crucial impediment to the flow of heat. When the rough edges of the surface interlock at the microscopic level, the interlocking is not perfect. This results in the creation of air gaps that act as a thermal RC circuit. Hence, the storage of heat increases the temperatures by a slight margin.

It is interesting to note there was no significant error in the simulation and the experiment. The developed COMSOL model and its results would be essential for the researchers and the students who are working in the area of power electronics which deals with thermal modeling and circuits.

7

Future Work and Recommendations

The model developed by using the procedure in Chapter 3, has shown that placing a rectifier over the receiver pad used for WPT can solve the constraints like thermal management, compactness and bulkiness. Although this model has been effective, there are still room for certain improvements which can be implemented to further enhance the models capability to be applicable in more diverse applications. These recommendations are the following.

1. The working model developed in this thesis is for the power level of 3.3 KW where the application is for light vehicles. But there must be a working model for higher power ranges like SUVs and trucks where there the case of the forced cooling must be considered parameters like air velocity, humidity and other external weather conditions.
2. The losses considered in the model are mainly coming from I^2R of the litz wire and the diodes. However, in reality, the losses due to the AC resistance, the eddy currents in the aluminum shield, the losses in the ferrite, must be also considered.
3. The same model designed in COMSOL to understand the heat distribution in the receiver can also be applied when the heat flow is different. In the case of the receiver pad, the natural convection of heat flow is used. On the other hand, in the case of the transmitter, the pad is located under the ground. The thermal analysis of the underground power electronics will be different as there is a possibility of no natural convection, and the usage of external coolingmight be necessary
4. The performance of the system decreases over time. Hence, the aging process of the different components in the receiver pad and the diode rectifier must be examined. The insulation of the Litz wires becomes less effective over time because of the heat produced due to the flow of current over time. Moreover, it could be studied how the diodes degrade over time and the impact on the thermal dissipation.
5. Investigating the effect of air gaps in the transfer of heat in a WPT system.

A

Appendix A

Comparison of losses in MATLAB vs LT spice

MATLAB				
V_{out}		290	350	400
V_{in}		493.79	494.58	495.24
I_m	RMS	3.8928	4.6864	5.3477
	AVG	2.4783	2.9834	3.4044
$P_{m,loss}$		8.3151	9.5054	10.5909
I_{L1}	RMS	5.5053	6.6275	7.5627
	AVG	0	0	0
P_{L1}		19.1623	27.7707	36.1608
P_{C1}		1.2123	1,757	2.2878
I_{L2}	RMS	9.1634	9.1634	9.1634
	AVG	0	0	0
P_{L2}		35.8404	35.8404	35.8404
P_{C2}		3.3587	3.3587	3.3587
I_{diode}	RMS	6.4795	6.4795	6.4795
	AVG	4.125	4.125	4.125
P_{diode}		5.3299	5.3299	5.3299
I_{out}		8.25	8.25	8.25
P_{out}		2392.5	2887.5	3300
$efficiency$		95.89	96.22	96.38

Table A.1: theoretical results of parameters after calculation in MATLAB

		VOLTAGE SOURCE			LOAD RESISTOR		
V_{out}		290	350	400	290	350	400
V_{in}		493.79	494.58	495.24	493.79	494.58	495.24
I_m	RMS	3.9744	4,7663	5.4267	3.9426	4.7167	5.3472
	AVG	2.5361	3.0435	3.4664	2.5157	3.0117	3.4154
$P_{m,loss}$		8.3151	9.5054	10.5909			
I_{L1}	RMS	5.6181	6.7377	7.6711	5.5731	6.6462	7.5586
	AVG	2.17E-06	1.05E-05	9.88E-06	1.02E-05	4.30E-05	5.99E-05
P_{L1}		19.956	28.701	37.205	19.637	27.927	36,122
P_{C1}		1.2626	1.8159	2.3539	1.2424	1.7669	2.2853
I_{L2}	RMS	9.1438	9.143	9.1425	9.14161	9.1458	9.146
	AVG	3.00E-07	1.79E-05	2.41E-05	-1,48E-07	1.60E-06	1.17E-06
P_{L2}		35.6876	35.68	35.677	35.705	35.703	35.704
P_{C2}		3.3443	3.3438	3.3434	3.346	3.3459	3.346
I_{diode}	RMS	6.4653	6.4647	6.4643	6.467	6.4668	6.4668
	AVG	4.1326	4.1309	4.1292	4.1337	4.1324	4.131
P_{diode}		5.3452	5.3428	5.3425	5.3463	5.343	5.3397
I_{out}		8.265	8.2617	8.2583	8.2519	8.1929	8.1768
P_{out}		2417.4	2912.1	3323.8	2393.6	2847,6	3241,7
$efficiency$		96.518	96.7314	96.808	96.28	96.306	96.807

Table A.2: theoretical results of parameters after calculation in LTSPICE

B

Appendix-B

MATLAB program for the calculation of thermal conductivity and the density of the litz layer.

```
clc
clear
L=16.7875;
D=2.5e-3;
%%%%%%%%%%%%%%%%%%%%%%thermal conductivity%%%%%%%%%%%%%%%%%%%%%%%%%%%%%%
delta_x=2.5e-3;
he_2=350e-3;
le_2=545e-3;
li_2=245e-3;
hi_2=50e-3;
N2=20;
g=(le_2-li_2-N2*D)/20;%250e-3/20;
k=0.02735;
%%%%%%%%%%%%%%%%%%%%%%%%%%%%density%%%%%%%%%%%%%%%%%%%%%%%%%%%%%%%%%%%
V_coil =pi*D^2*L/4;
V_frame=(le_2*he_2-li_2*hi_2)*2.5e-3;
V_air=V_frame-V_coil;
P=8920*V_coil*9.81/(le_2*he_2);
d1=8920;
d2=1225;
m1=d1*V_coil;
m2=d2*V_air;
d3=(m1+m2)/(V_coil+V_air);
%%%%%%%%%%%%%%%%%%%%Aluminium%%%%%%%%%%%%%%%%%%%%%%%%%%%%%%%%%%%%
d_AL=2700;
V_AL=570e-3*370e-3*2e-3;
m_AL=d_AL*V_AL;
%%%%%%%%%%%%%%%%%%%%Ferrite%%%%%%%%%%%%%%%%%%%%%%%%%%%%%%%%%%%%%
d_Fe=4900;
V_Fe=43*13e-3*28*13e-3*4.1e-3;
m_Fe=V_Fe*d_Fe;
%%%%%%%%%%%%%%%%%%wood b/n ferrite and AL %%%%%%%%%%%%%%%%%%%%%%%%%%%%%%%%%%
d_wood=800;
V_wood=585e-3*385e-3*2e-3;
m_wood=V_wood*d_wood;
%%%%%%%%%%%%%%%%%wood b/n ferrite and litz %%%%%%%%%%%%%%%%%%%%%%%%%%%%%%%%
```

```
d_wood2=800;
V_wood2=585e-3*385e-3*2e-3;
m_wood2=V_wood*d_wood;
%%%%%%%%%%%%%%%%%%%%%%thermal conductivity
    %%%%%%%%%%%%%%%%%%%%%%%%%%%%%%%%%%%
V_c=(2.3/0.071)*pi*(0.071e-3)^2*L/4;
V_i=V_coil-V_c;
v_c=V_c/(V_i+V_c);
d_litz=(V_c*d1+V_i*1780)/(V_c+V_i);
ki=1.25;
Ke=ki*((1+v_c)*385+(1-v_c)*ki)/((1-v_c)*385+(1+v_c)*ki);
%%%%%%%%%%%%%%%%%%%%%%%%%%%%%z thermal conductivity%%%%%%%%%%%%%%%%%%%%
CSA_wirez=20*2*pi*D^2/4;
CSA_layerz=he_2*delta_x;
CSA_gapz=hi_2*delta_x;
CSA_airz=CSA_layerz-CSA_wirez;
r_copperz=delta_x/(Ke*CSA_wirez);
r_airz=delta_x/(k*CSA_airz);
r_gapz=delta_x/(k*CSA_gapz);
r_matz=r_copperz*r_airz/(r_copperz+r_airz);
r_layerz=1/(1/r_airz+1/r_copperz+1/r_gapz);
t_matz=delta_x/(r_matz*CSA_layerz);
%%%% %%%%%%%%%%%%%%%%%%%%%% x thermal conductivity%%%%%%%%%%%%%%%%%%%%%
% CSA_wirex=20*2*2*pi*D/2*L;
% CSA_layerx=(he_2-hi_2)*delta_x;
% CSA_gapx=hi_2*delta_x;
% CSA_airx=CSA_layerx-CSA_wirex;
% r_copperx=(le_2)/(Ke*CSA_wirex);
% r_airx=le_2/(k*CSA_airx);
% r_gapx=li_2/(k*CSA_gapx);
% r_matx=r_copperx*r_airx/(r_copperx+r_airx);
% r_layerx=1/(1/r_airx+1/r_copperx+1/r_gapx);
% t_matx=le_2/(r_matx*CSA_layerx);
%%%%%%%%%%%%%%%%%%%%%%%%%%% y thermal conductivity%%%%%%%%%%%%%%%%%%%%%
% CSA_wirey=20*2*2*pi*D/2*L;
% CSA_layery=(le_2-li_2)*delta_x;
% CSA_gapy=li_2*delta_x;
% CSA_airy=CSA_layery-CSA_wirey;
% r_coppery=(he_2)/(Ke*CSA_wirey);
% r_airy=he_2/(k*CSA_airy);
% r_gapy=hi_2/(k*CSA_gapy);
% r_maty=r_coppery*r_airy/(r_coppery+r_airy);
% r_layery=1/(1/r_airy+1/r_coppery+1/r_gapy);
% t_maty=he_2/(r_maty*CSA_layery);
% A=[t_matx t_maty t_matz];
```

C

Appendix-C

MATLAB program for the calculation of weights of the receiver layers and heatsink

```
l=0.585;
w=0.385;
%%%%%%%%%%%%%%%%%%%%%%%%%%coil layer%%%%%%%%%%%%%%%%%%%%%%%%%%%%%%%%%%%%%%%%%%
le_2=0.545;
he_2=0.350;
li_2=0.245;
hi_2=0.05;
D=2.5e-3;
L=16.7875;
t=D;
V_coil=pi*D^2*L/4;
V_frame=(le_2*he_2-li_2*hi_2)*t;
d_litz=8920;
m_litz=d_litz*V_coil;
%%%%%%%%%%%%%%%%%%%%%%%%%ferrite layer%%%%%%%%%%%%%%%%%%%%%%%%%%%%%%%%%%%%%%%%%%
d_Fe=2700;
l_Fe=43*12e-3;
h_Fe=28*12e-3;
t_Fe=4.1e-3;
V_Fe=l_Fe*h_Fe*t_Fe;
m_Fe=V_Fe*d_Fe;
%%%%%%%%%%%%%%%%%%%%%%%%%%%%AL layer%%%%%%%%%%%%%%%%%%%%%%%%%%%%%%%%%%%%%%%%%%%%
d_AL=2734;
l_AL=0.57;
h_AL=0.37;
t_AL=2e-3;
V_AL=l_AL*h_AL*t_AL;
m_AL=d_AL*V_AL;
%%%%%%%%%%%%%%%%%%%%%%%%%%wood layer%%%%%%%%%%%%%%%%%%%%%%%%%%%%%%%%%%%%%%%%%
d_wood=250;
t_wood=4e-3;
V_wood=l*w*t_wood;
m_wood=V_wood*d_wood;
%%%%%%%%%%%%%%%%%%%%%%%%%%wood frame%%%%%%%%%%%%%%%%%%%%%%%%%%%%%%%%%%%%%%%%%
m_LitzFrame=d_wood*(t-0.5e-3)*(l-le_2)*(w-he_2);
```

```
m_ALFrame=d_wood*t_AL*(l-l_AL)*(w-h_AL);
d_acrylic=1190;
m_acrylicframe=d_acrylic*(t_Fe-1.1e-3)*(l-l_Fe)*(w-h_Fe);
%%%%%%%%%%%%%%%%%%%%%%%%%%%%heatsink%%%%%%%%%%%%%%%%%%%%%%%%%%%%%%%%%%%%
f1=0.6;
f2=0.7;
l_heatsink=f1*0.36;
w_heatsink=f2*0.21;
t_heatsink=4e-3;
V_heatsink=l_heatsink*w_heatsink*t_heatsink;
m_heatsink=V_heatsink*d_AL;
%%%%%%%%%%%%%%%%%%%%%%%%%% 2 cases%%%%%%%%%%%%%%%%%%%%%%%%%%%%%%%%%%%%%
m1=2.5*m_wood+m_litz+m_Fe+m_AL+m_LitzFrame+m_ALFrame+m_acrylicframe+
    m_heatsink;
m2=2.5*m_wood+m_litz+m_Fe+m_AL+m_LitzFrame+m_ALFrame+m_acrylicframe;
```

D

Appendix D

MATLAB program for the plot of T_j and T_t vs the length of the heatsink

```
clc
clear
l=360;
f1=[0.4,0.5,0.6,0.7,0.8,0.9,1];
X=readtable('\\tudelft.net\student-homes\p\gpillai\Desktop\Thesis\Temperature.xlsx');
T_j_1=X{2:7:44,3};
T_j_2=X{3:7:45,3};
T_j_3=X{4:7:46,3};
T_j_4=X{5:7:47,3};
T_j_5=X{6:7:48,3};
T_j_6=X{7:7:49,3};
T_j_7=X{8:7:50,3};
%plot(w*f2,T_j_7)
T_t_1=X{2:7:44,4};
T_t_2=X{3:7:45,4};
T_t_3=X{4:7:46,4};
T_t_4=X{5:7:47,4};
T_t_5=X{6:7:48,4};
T_t_6=X{7:7:49,4};
T_t_7=X{8:7:50,4};
%%%%%%%%%%%%%%%%%%%%%%%%%temp vs length %%%%%%%%%%%%%%%%%%%%%%%%%%%%%%%%%%%%%%%%%%%%%%%
a1=plot(l*f1,T_t_1);
M1="f2=0.4";
hold on
a2=plot(l*f1,T_t_2);
M2="f2=0.5";
hold on
a3=plot(l*f1,T_t_3);
M3="f2=0.6";
hold on
a4=plot(l*f1,T_t_4);
M4="f2=0.7";
hold on
a5=plot(l*f1,T_t_5);
M5="f2=0.8";
hold on
```

```
a6=plot(l*f1,T_t_6);
M6="f2=0.9";
hold on
a7=plot(l*f1,T_t_7);
M7="f2=1";
hold off
title('Top case temperature of the diodes vs Length');
ylabel('Temperature (degrees)');
xlabel('Length of the heatsink(mm)');
ylim([41,47])
xlim([l*f1(1),l*f1(7)])
legend([a1,a2,a3,a4,a5,a6,a7],[M1,M2,M3,M4,M5,M6,M7]);
```

MATLAB program for the plot of T_j and T_t vs the width of the heatsink

```
clc
clear
w=210;
f2=[0.4,0.5,0.6,0.7,0.8,0.9,1,1.1,1.2,1.3,1.4,1.5,1.6,1.7,1.76];
X=readtable('\\tudelft.net\student-homes\p\gpillai\Desktop\Thesis\Temperature.xlsx');
T_j_1=X{51:65,3};
T_j_2=X{9:15,3};
T_j_3=X{16:22,3};
T_j_4=X{23:29,3};
T_j_5=X{30:36,3};
T_j_6=X{37:43,3};
T_j_7=X{44:50,3};
%plot(w*f2,T_j_7)
T_t_1=X{51:65,4};
T_t_2=X{9:15,4};
T_t_3=X{16:22,4};
T_t_4=X{23:29,4};
T_t_5=X{30:36,4};
T_t_6=X{37:43,4};
T_t_7=X{44:50,4};
%%%%%%%%%%%%%%%%%%%%%%%%%%%%%%temp vs width %%%%%%%%%%%%%%%%%%%%%%%%%%%%%%%%%%%%%%%%%%%%%%%%%%%%%%%%%%%
a1=plot(w*f2,T_t_1);
M1="f1=0.4";
% hold on
% a2=plot(w*f2,T_j_2);
% M2="f1=0.5";
% hold on
% a3=plot(w*f2,T_j_3);
% M3="f1=0.6";
% hold on
% a4=plot(w*f2,T_j_4);
% M4="f1=0.7";
% hold on
% a5=plot(w*f2,T_j_5);
% M5="f1=0.8";
% hold on
% a6=plot(w*f2,T_j_6);
% M6="f1=0.9";
% hold on
% a7=plot(w*f2,T_j_7);
```

```
% M7="f1=1";
% hold off
title('Junction temperature of the diodes vs Width');
ylabel('Temperature (degrees)');
xlabel('Width of the heatsink(mm)');
ylim([40,50])
xlim([w*f2(1)+5,w*f2(7)+5])
%legend([a1,a2,a3,a4,a5,a6,a7],[M1,M2,M3,M4,M5,M6,M7]);
%%%%%%%%%%%%%%%%%%%%%%%%%temp vs length
    %%%%%%%%%%%%%%%%%%%%%%%%%%%%%%%%%%%%%%%%%%%%%%%%%%
```

Bibliography

[1] H. Feng et al. “Advances in High-Power Wireless Charging Systems: Overview and Design Considerations”. In: *IEEE Transactions on Transportation Electrification* 6.3 (2020), pp. 886–919. DOI: `10.1109/TTE.2020.3012543`.

[2] D. Patil et al. “Wireless Power Transfer for Vehicular Applications: Overview and Challenges”. In: *IEEE Transactions on Transportation Electrification* 4.1 (2018), pp. 3–37. DOI: `10.1109/TTE.2017.2780627`.

[3] X. Mou et al. “Survey on magnetic resonant coupling wireless power transfer technology for electric vehicle charging”. In: *IET Power Electronics* 12.12 (2019), pp. 3005–3020. DOI: `10.1049/iet-pel.2019.0529`.

[4] V. Cirimele et al. “Inductive Power Transfer for Automotive Applications: State-of-the-Art and Future Trends”. In: *IEEE Transactions on Industry Applications* 54.5 (2018), pp. 4069–4079. DOI: `10.1109/TIA.2018.2836098`.

[5] S. Li and C. C. Mi. “Wireless Power Transfer for Electric Vehicle Applications”. In: *IEEE Journal of Emerging and Selected Topics in Power Electronics* 3.1 (2015), pp. 4–17. DOI: `10.1109/JESTPE.2014.2319453`.

[6] V. Shevchenko et al. “Compensation Topologies in IPT Systems: Standards, Requirements, Classification, Analysis, Comparison and Application”. In: *IEEE Access* 7 (2019), pp. 120559–120580. DOI: `10.1109/ACCESS.2019.2937891`.

[7] S. Bandyopadhyay et al. “Comparison of Magnetic Couplers for IPT-Based EV Charging Using Multi-Objective Optimization”. In: *IEEE Transactions on Vehicular Technology* 68.6 (2019), pp. 5416–5429. DOI: `10.1109/TVT.2019.2909566`.

[8] W. Zhang and C. C. Mi. “Compensation Topologies of High-Power Wireless Power Transfer Systems”. In: *IEEE Transactions on Vehicular Technology* 65.6 (2016), pp. 4768–4778. DOI: `10.1109/TVT.2015.2454292`.

[9] Chwei-Sen Wang, G. A. Covic, and O. H. Stielau. “General stability criterions for zero phase angle controlled loosely coupled inductive power transfer systems”. In: *IECON’01. 27th Annual Conference of the IEEE Industrial Electronics Society (Cat. No.37243)*. Vol. 2. 2001, 1049–1054 vol.2. DOI: `10.1109/IECON.2001.975925`.

[10] W. Ned Mohan T.M.Undeland. *Power Electronics*. John Wiley & Sons, Ltd, 1998, pp. 16–25. ISBN: 0-471-58408-8.

[11] S. G.R. Liu. *The Finite Element Method:A Practical Course*. Butterworth-Heinemann, 2003, pp. 1–2. ISBN: 0 7506 5866 5.

[12] J. Proulx. *Component Creation in FloTHERM-C4D10120D SiC Diode*. C4D20120H Model setup. 2016.

[13] *Heat Transfer Module User’s Guide*. 1998, pp. 270–273.

[14] A.Bejan. *Heat Transfer*. 6th ed. John Wiley & Sons, Ltd, 2003, pp. 561–562. ISBN: 0-471-39015-1.

[15] E. A. Jones and M. de Rooij. “High-Power-Density GaN-Based Converters: Thermal Management Considerations”. In: *IEEE Power Electronics Magazine* 6.4 (2019), pp. 22–29. DOI: `10.1109/MPEL.2019.2946699`.

[16] V. J.Pyrhonen T.Jokinen. *Design of Rotating Electrical Machines*. John Wiley & Sons, Ltd, 2008, pp. 477–479. ISBN: 978-0-470-69516-6.

[17] R. Wrobel, S. Ayat, and J. L. Baker. “Analytical methods for estimating equivalent thermal conductivity in impregnated electrical windings formed using Litz wire”. In: *2017 IEEE International Electric Machines and Drives Conference (IEMDC)*. 2017, pp. 1–8. DOI: `10.1109/IEMDC.2017.8002003`.

[18] A. T.L.BERGMAN. *Introduction to Heat Transfer*. 6th ed. John Wiley & Sons, Ltd, 2011, pp. 573–574. ISBN: 978-0470-50196-2.